

An aerial photograph of a river delta, likely the Mississippi River delta, showing a complex network of channels and distributaries. The image is overlaid with a teal color gradient, which is darker in the center and lighter towards the edges. The text is positioned in the upper left quadrant of the image.

**TIME-DEPENDENT LINEARIZED FRICTION:  
A DEVELOPMENT ON LORENTZ'  
ENERGY ARGUMENTS**

**CHRIS PITZALIS**

© MSc Thesis – Chris Pitzalis  
© Cover Photo – ESA

# UNIVERSITY OF TWENTE.

MSc THESIS

---

## Time-dependent linearized friction: a development on Lorentz' energy argument

---

*Author:*  
Chris PIZALIS

*Supervision:*  
P.C. ROOS  
G. LIPARI  
S.J.M.H. HULSCHER

June 2, 2017  
Final version

*“Fourier is a mathematical poem.”*

Sir William Thomson  
(later known as Lord Kelvin)



Joseph Fourier



Lord Kelvin

# Contents

<b>Preface</b>	<b>6</b>
<b>Summary</b>	<b>7</b>
<b>1 Introduction</b>	<b>8</b>
1.1 Background . . . . .	8
1.2 Objective and research questions . . . . .	12
1.3 Methodology and report outline . . . . .	13
<b>2 Model formulation</b>	<b>15</b>
2.1 Network geometry . . . . .	15
2.2 Hydrodynamics . . . . .	18
2.3 Time-dependent friction coefficient $r_j(t)$ . . . . .	19
<b>3 Solution method</b>	<b>23</b>
3.1 Spectral approach . . . . .	23
3.2 Decoupling problem . . . . .	25
3.3 Solving problem . . . . .	27
3.4 Iteration process . . . . .	27
<b>4 Results: Single channel</b>	<b>29</b>
4.1 Synthetic forcing . . . . .	29
4.2 Tide-surge interaction with synthetic forcing . . . . .	32
<b>5 Results: Wadden Sea network</b>	<b>34</b>
5.1 Hindcasting Sinterklaasstorm 2013 . . . . .	34
<b>6 Discussion</b>	<b>41</b>
6.1 General model simplifications and assumptions . . . . .	41
6.2 Solution method . . . . .	42
6.3 Interpretation of results and insights from $r_j(t)$ . . . . .	42
6.4 Tide-surge interaction . . . . .	44
<b>7 Conclusion and recommendations</b>	<b>45</b>
<b>Bibliography</b>	<b>48</b>
<b>List of symbols</b>	<b>49</b>
<b>Appendices</b>	<b>50</b>
<b>A Example linear algebra matrices M, C and A</b>	<b>51</b>

# Preface

Before you lies my thesis report ‘*Time-dependent linearized friction: a development on Lorentz’ energy argument*’. This report, together with my colloquium next Friday June 9, will hopefully finalize my graduation period by receiving the Masters degree for Civil Engineering.

Since I can remember, I have always had an passion for mathematics. I had high hopes that this project would challenge me mathematically. I am pleased to say it did. Besides that, I was fortunate enough that this project combined more of my interests; the hydrodynamics belonging to the dynamic environment of the Wadden Sea and building simulation models from scratch.

I would like to thank Pieter (P.C. Roos) and Koen (K.R.G. Reef) especially. Pieter for the assignment and the guidance. Koen for his previous work on this subject. I would like to thank both, Suzanne (S.J.M.H. Hulscher) and Giordano (G. Lipari) for the useful discussions and the constructive criticism. It has been a joyful year, and that is thanks to you. I also would like to thank my friends, family and classmates for their interest in my graduation project.

I hope everyone enjoys my thesis report. Feel free to contact me with any question (chrispitzalis@gmail.com).

Chris Pitzalis

Enschede, June 2, 2017

# Summary

In 1918 the State Committee, chaired by professor Hendrik Antoon Lorentz, was commissioned to investigate the consequences of constructing the Dutch closure dam the Afsluitdijk. The Committee's assignment was to determine to what extent one may expect the water levels to rise during storm events. The Committee developed a process-based one-dimensional network model simulating separately the tidal and surge water levels. Essential was the energy argument applied to linearize the quadratic friction parametrization of the tidal model. Lorentz determined a steady friction coefficient by equaling the linearized energy dissipation to the quadratic.

Recently, Reef et al. (2016) continued the State Committee's pioneering work by reconstructing their storm model and extending it to a non-stationary model which simulates the time-dependent forcing in the frequency domain. This allowed them to investigate the transient behaviour of Wadden Sea storms. Concluding their research, Reef et al. argue that when the flow velocity is lower than the maximum velocity, their steady friction model overestimates energy dissipation. They propose for future research a time-dependent friction coefficient, in which a varying velocity scale may be better suited with the varying wind stress and tidal forcing.

This study implemented a time-dependent friction coefficient. We have done this in a linearized fashion by applying a convolution sum to the frictional term in the momentum equation. This couples each frequency in the spectrum, which is a large advantage since it enables interaction between frequencies (e.g. the interaction between tide and surge).

We have performed simulations for an idealized single channel and the Wadden Sea network. The qualitative behaviour is good. The single channel simulations show that when the steady friction coefficient overestimates energy dissipation, the time-dependent friction model feels less friction. The steady friction simulations display overdamping and a phase lag compared to the time-dependent friction model. We observe significant interaction between tide and surge. The peak surface elevation of the simultaneously forced model is nearly 20% lower than when forced separately. The reduction is likely to be a result of the larger tidal velocities, which in turn result in more friction. The simulations for the Wadden Sea network are performed for the 2013 Sinterklaasstorm. The simulations are in good agreement with measurements. The differences are often within 10 centimetres. During storm there are some outliers of at most 30 centimetres.

The solution method applied in this study is promising, especially for research on interaction (e.g. tidal constituents or tide and surge) with idealized analytical network models.

# Chapter 1

## Introduction

Hydrodynamic models are widely used, for instance in scenario analysis. The State Committee (1926) was the first to successfully set up a large scale hydrodynamic model. Using their one-dimensional tidal and storm network model they investigated the hydrodynamic impact of constructing the closure dam the Afsluitdijk. One of the team leaders (Thijsse, 1972) later recalled that the calculations of the existing tide took one month for two persons. Essential in State Committee's tidal model was the energy argument applied to linearize the quadratic friction. This resulted in a steady friction coefficient with which in tidally-averaged sense equalled the energy dissipation to the quadratic friction.

Reef et al. (2016) extended the State Committee's stationary storm model with time-dependent wind forcing. While doing so, they showed that the State Committee's idealized model is still valuable for rapid assessment. The model runs take in this digital era only seconds to minutes. Reef et al. (2016) applied a steady friction coefficient to their storm model. However, the less predictable behaviour of storms made it unclear how to specify this coefficient accurately.

This study continues with extending the State Committee's tidal channel network model. We propose a new bottom friction parametrization that captures the non-linear time-dependent behaviour. Our report offers a detailed description of the full model and its extension. We provide simulation results for a single channel with focus on physical processes and hindcast the Dutch Wadden Sea tidal channel network with focus on model performance during storm conditions.

This chapter provides background information on the topic (section 1.1), further elaboration of our objective (section 1.2), the research questions (section 1.2), a detailed description of the modelling domain (section 1.1.5), an introduction to our methodology (section 1.3) and a report outline (section 1.3).

### 1.1 Background

This section starts with previous work on network models, including State Committee (1926) and Reef et al. (2016) (subsection 1.1.1). We discuss Lorentz' linearized bottom friction parametrization in subsection 1.1.2, which is the inspiration to our parametrization. Information on tide-surge interaction is provided in subsection 1.1.3. Our parametrization enables interaction. Subsection 1.1.4 provides information on extra-tropical storms. The Wadden Sea is located in the mid-latitudes which is dominated by extratropical storms.

#### 1.1.1 Network modelling

Our research focuses on idealized analytical network models that are one-dimensional and based on the depth-averaged shallow water equations. The State Committee (1926) and Reef et al. (2016) considered such models.

### **Wadden Sea network model by the State Committee (1926)**

Headed by Hendrik Antoon Lorentz, the State Committee was commissioned in 1918 to investigate the hydrodynamic consequences of constructing a closure dam which would disconnect the Dutch Zuiderzee<sup>1</sup> from the Wadden Sea. In 1926 the State Committee developed a process based model that was able to simulate the tidal and storm water levels for the Dutch Wadden Sea reasonably well. The possible hydrodynamic effects were investigated with this model and the parliament subsequently decided to construct the so-called Afsluitdijk.

The idealized model by the State Committee (1926) applied several simplifications. The model simulates the tidal and surge water levels separately and therefore the effects of tide-surge interaction were not incorporated. The model considered a network of one-dimensional channels that allowed only for along-channel flow. Cross-channel flow was neglected as it was assumed to be limited. The dominance of along-channel flow results from the tidal channel bathymetry of the Wadden Sea. The network of channels were set up to mimic the actual (tidal) channels. The quadratic bottom friction parametrization of the tidal model was linearized (see subsection 1.1.2). This, and the exclusion of other non-linear effects as a further simplification, made an analytical solution feasible. The storm model considered a unidirectional constant wind stress, both uniform in space and time. Contrary to the tidal model, the storm model was stationary.

### **Extended non-stationary storm model by Reef et al. (2016)**

Reef et al. (2016) studied the transient behaviour of storm surges in the Wadden Sea. They added inertia and a time-dependent wind stress to the storm surge model by the State Committee (1926).

Similar to the State Committee, Reef et al. considered the storm to be unidirectional and the wind stress spatially uniform. The time-dependent wind stress field was decomposed into time-dependent sinusoidal signals by using the Discrete Fourier Transformation. In comparison to the tidal model by the State Committee, Reef et al. applied a slightly different linearized bottom friction parametrization. Both parametrizations are discussed further in subsection 1.1.2.

The simulation results were reasonably accurate. Reef et al. found that the water level peaks after the moment of maximum wind stress. This was attributed to the inclusion of inertia, which was not part of the stationary storm model by the State Committee.

Reef et al. also reproduced the tidal model by the State Committee, which had similar results.

### **Other developments**

Many network models have been created since the State Committee, both complex and idealized that were either numerical or analytical. Ridderinkhof (1988a,b) studied for instance tidally-driven residual flows in the western Dutch Wadden Sea with a one-dimensional analytical model and an extension of a two-dimensional numerical model. Bakker and de Vriend (1995) studied possible resonance and the morphological stability of tidal basins in case of a modification to the tidal basins. Their analytical model was based on the linearized friction model by the State Committee. Hill and Souza (2006) created an algorithm which provides rapid assessment of linear tidal dynamics for an arbitrarily complex network of tidal channels. Their work is an extension of their previous analytical solution for a single channel (Souza and Hill, 2006). Alebregtse and de Swart (2016) incorporated non-linearities in their network model by using a perturbation expansion.

---

<sup>1</sup>Nowadays the Zuiderzee is split into two fresh water lakes, known as the Markermeer and IJsselmeer.

### 1.1.2 Lorentz' linearized friction coefficient $r$

Energy dissipation due to bottom friction is proportional to the quadratic velocity. The bed shear stress is thus often parametrized by

$$\tau_{b,quad,j} = c_d \rho |u_j| u_j,$$

with channel number  $j$ , channel-dependent bed shear stress  $\tau_{b,quad,j}$ , water density  $\rho$ , dimensionless drag coefficient  $c_d$  that is depth and spatially averaged and along-channel and cross-sectionally averaged velocity  $u_j$ . The quadratic velocity poses mathematical difficulties when seeking analytical solutions. To bypass this problem, Lorentz (1922) proposed a linear parametrization

$$\tau_{b,lin,j} = r_j \rho u_j,$$

with bottom friction coefficient  $r_j$  in metres per second. The friction coefficient – that is channel dependent, steady and spatially uniform within the channel – follows from equalling the quadratic energy dissipation to the linear dissipation (Lorentz, 1922). To facilitate the derivation, Lorentz assumed a sinusoidal tidal velocity signal  $u_j = \hat{u}_j \cos \omega t$ , with time  $t$ , tidal velocity amplitude  $\hat{u}_j$  and tidal frequency  $\omega$ . Lorentz neglected tidal asymmetry, this proved to be of negligible influence since the tidal calculations were up to a few centimetres accurate. The drag coefficient  $c_d$  was described as  $g/C^2$  with gravitational acceleration  $g$  and Chezy smoothness coefficient  $C$  ( $m^{1/2}s^{-1}$ ). The derivation of  $r_j$  using the energy argument above over a full tidal cycle is given by

$$r_j \int_{-\frac{\pi}{\omega}}^{+\frac{\pi}{\omega}} \hat{u}_j^2 \cos^2 \omega t \, dt = \frac{g}{C^2} \int_{-\frac{\pi}{\omega}}^{+\frac{\pi}{\omega}} \hat{u}_j^3 \cos^3 \omega t \, dt,$$

leading to  $r_j = \frac{8}{3\pi} \frac{g \hat{u}_j}{C^2}$ .

Note that the friction coefficient  $r_j$  is dependent on the velocity amplitude and with that the solution to  $u_j$ . In turn is the solution dependent on the friction coefficient. Lorentz solved this fundamental difficulty by pre-determining the velocity amplitude from measurements. The tidal model by Reef et al. (2016) showed that approximate equal simulation results were obtained when the velocity amplitude resulted from converging iterations.

#### Storm coefficient by Reef et al. (2016)

Where the tidal velocity profile has a characteristic sinusoidal shape, the velocity profile during storm conditions has not. Henceforth, the energy argument is not that easily applied. Reef et al. used for their storm model the friction coefficient

$$r_j = \frac{g u_{a,j}}{C_j^2}. \tag{1.1}$$

Due to the less predictable behaviour of storms, it was unclear which value for  $u_{a,j}$  would approximately equal the linear dissipation to the quadratic. In the storm model  $u_{a,j}$  was taken equal to the average of the maximum velocity at both channel ends. The coefficient was obtained through iterations. To incorporate the effect of decreasing friction with increasing depth, the smoothness coefficient  $C_j$  as  $h_j^{1/6} M_n^{-1}$  with Manning coefficient  $M_n$  in  $s \, m^{-1/3}$  and mean depth  $h_j$ . The Manning relation is often described with the hydraulic radius instead of the mean depth. However, since the tidal channels in the Wadden Sea have an much larger width than depth, then the hydraulic radius is approximately the mean depth.

### **Empirical Manning coefficient**

The friction coefficient by Reef et al. applies an empirical parameter, namely the Manning coefficient  $M_n$ . These type of parameters are based on observations or experience. This is in contrast to physical parameters that describe a physical property, for instance the density of a fluid. The Manning coefficient incorporates the local channel conditions. This includes for instance (I) bed resistance like bed material and bed forms and (II) bank resistance due to vegetation, all conditions that may change over time. Henceforth, the Manning coefficient is a rough estimation of local conditions. Chow (1959) has estimated the Manning coefficient for many conditions and is therefore often referenced, also by Reef et al.

### **1.1.3 Tide-surge interaction**

It has long been recognized that tide-surge interaction must exist since residual maxima generally occur on the rising tide. Doodson (1929) and Rossiter (1961) noted this in the Thames estuary, Prandle and Wolf (1978) and Horsburgh and Wilson (2007) confirmed this statistically. Brown and Wolf (2009) observed that wind stress peaks are not in phase with surge peaks and that residual is significantly larger at low water. Prandle and Wolf mention that interaction frequently leads to a reduction.

Prandle and Wolf (1978) simulated the quadratic friction and shallow water interaction mechanisms in the Thames estuary. Their results showed that quadratic friction is the dominant mechanism. In shallow water the friction term becomes increasingly important as bottom friction is inversely dependent on water depth.

Wind stress is more effective at raising the sea surface in shallow water (Pugh, 1987). Therefore the timing of the wind event with respect to spring/neap phase and tidal high/low stage is determinant for the size of interaction (Horsburgh and Wilson, 2007; Brown et al., 2010). Considering this, interaction can increase as well as decrease surge levels; low tide will increase surge levels as the water depth is below the normal depth, whereas high tide will have the reversed effect.

### **1.1.4 Extra-tropical storms**

Sea-level variations are chiefly caused by a tidal and meteorological component. The meteorological component consists of atmospheric pressure and wind stress, two closely related phenomena. Atmospheric pressure acts vertically on the sea surface. Horizontal pressure differences result in differences in sea level elevation; as pressure decreases, sea level will increase (Pugh, 1987). Large spatial gradients in atmospheric pressure result in strong winds. These winds act as a horizontal drag force on the sea surface (i.e. wind stress). Sea level elevation due to atmospheric pressure is only small and extreme surge in the Wadden Sea generally exceeds the tidal elevation. The order of importance is thus respectively wind stress, tidal forcing and atmospheric pressure.

The Wadden Sea is located in the mid-latitudes, a region that is subject to extratropical storms. These storms occur predominantly in winter when the horizontal temperature gradients are strong (Renggli, 2011). Forced by low pressure, storms have radii between a few hundreds and thousands of kilometres and travel eastward due to the polar jet stream entering the North Sea in the northern part. Influenced by the rotation of the earth (Coriolis effect), winds rotate counter-clockwise in the Northern Hemisphere along the isobars (Lipari and van Vledder, 2009; Klein, 2015; and references therein).

Due to the excessive size of storms, the Wadden Sea is generally affected by the southern part of a North Sea storm. This results in some key characteristics for the direction of the wind stress in the Wadden Sea (schematically displayed in Figure 1.1). As the south eastern quadrant of the storm approaches, the anticlockwise wind originates from the south and south-west. As the storm progresses easterly, the south western quadrant causes wind to originate

from the north-west and north. Due to this rotational behaviour positive surges can be well preceded by negative surges. The 2013 Sinterklaasstorm<sup>2</sup> displays this rotational behaviour, see wind measurements from the Vlieland station in Figure 2.7. Before peak wind speeds there is a rotational wind direction change from north to east to south.

### 1.1.5 Case description: the Wadden Sea

The Wadden Sea is a system of coupled tidal inlets that is characterized by a series of tidal inlets that separate the barrier islands and connect the open sea with the back-barrier bay (Figure 2.4). In the Dutch part of the Wadden Sea are five tidal inlets, namely from south-west to north-east Marsdiep-, Eierlandse gat-, Vlie-, Ameland- and Pinkegat-inlet. Sediment transport both going into and out of the back-barrier basin result in ebb- and flood deltas. This results in typical elevated tidal flats and deepened tidal channels. As a result the main flow goes through these tidal channels. In the back-barrier bay, tidal inlet systems can be both single systems or coupled systems. The tidal inlet systems of the Eierlandse Gat and Ameland have for instance a limited flow exchange with other systems, whereas the Marsdiep- and Vlie-inlet are connected by the streams Texelstroom and Vlietstroom. Tidal inlet systems are divided by tidal flats, this boundary is named the tidal divide or watershed.

Long term measurements confirmed that the Wadden Sea is dominated by tidal currents (Buijsman and Ridderinkhof, 2012; Wang et al., 2012). Wang et al. note that flow across the tidal divides is limited. Analysis by van Vledder and Adema (2007) of two winter storms in 2006-2007 showed that storms can increase water levels significantly and align currents with the wind direction. These flows are able to cross tidal divides.

## 1.2 Objective and research questions

The behaviour of storms is less predictable compared to tides. This made it unclear for Reef et al. what value would be appropriate as velocity scale for the bottom friction coefficient. Reef et al. applied the maximum velocity. As a result, the friction coefficient is overestimated when

<sup>2</sup> The name of the 2013 Sinterklaasstorm refers to the Dutch national holiday Sinterklaas. The storm occurred on the same date, that is December 5th. European meteorological services generally apply their own naming to storms. For instance, the 2013 Sinterklaasstorm is named by Germany Xaver and the United Kingdom uses Cameron.

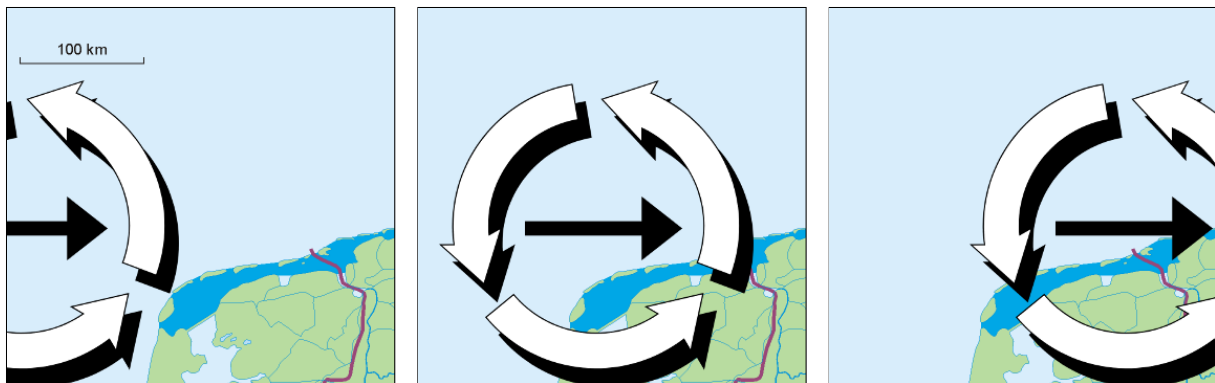


Figure 1.1: Schematic display of the rotational wind behaviour in the Wadden Sea (blue dyed). The storm displayed by the rotating arrows (not to scale) travels eastward (horizontal arrow) resulting, respectively in the figures from left to right, in wind originating from the south, the west and eventually the north. Wadden Sea background from Wikipedia.

the velocity is not equal to the maximum velocity. Reef et al. discuss this drawback and, as a recommendation for future research, propose a time-dependent friction coefficient:

$$\tau_{b,lin,j} = r_j(t)\rho u_j.$$

They suggest to solve the problem by applying a Fourier transformation and linear algebra.

The time-dependency of  $r_j(t)$  allows us to capture the nonlinear variation in bottom stress over the various stages in the storm event:  $r_j(t)$  will be large whenever the flow is strong and small when it is weak.

Our objective is to investigate the implementation of this time-dependent coefficient while retaining its attractive linear properties.

Besides implementing  $r_j(t)$ , we construct a non-stationary network model that is simultaneously forced by both tide and wind. Together with the time-dependent friction coefficient, this allows us to investigate the tide-surge interaction due to bottom friction.

The following research questions have been formulated to address the objective:

- 1. How can we implement a time-dependent bottom friction parametrization semi-analytically without losing its linear advantages?**
- 2. How do the simulation results with a time-dependent friction coefficient compare quantitatively and qualitatively with the steady coefficient for**
  - a) a single channel that is synthetically forced by wind, tide and both?
  - b) Lorentz' channel network forced by the 2013 Sinterklaasstorm?
- 3. What insights do the simulation results provide for tide-surge interaction?**

### 1.3 Methodology and report outline

The model formulation in **chapter 2** includes the governing linearized shallow water equations, the boundary conditions and the system's simultaneous tide and wind forcing. Besides, this first chapter discusses our time-dependent bottom friction coefficient that captures its essentially non-linear behaviour.

**Chapter 3** describes how the time-dependent friction coefficient is implemented linearly. The non-linear nature of both the friction coefficient and the forcing is modelled in the frequency domain. By applying the Discrete Fourier Transformation to the model input – which includes the time-dependent friction coefficient –, both the input and output are Fourier series. The additional frictional Fourier series – with respect to Reef et al.'s (2016) steady friction model – causes a product of two series. This results in a mathematical difficulty which is solved by translating the double Fourier series to a convolution sum of coupled frequencies. By using a matrix notation we apply linear algebra to decouple and solve the problem. The resulting product is a linearized non-stationary model that allows for non-linear energy dissipation. The beforehand unknown friction coefficient is determined by an iterative process.

We use our model to investigate the following aspects:

- Our results should be equal to Reef et al.'s when applying the same friction coefficient. The Wadden Sea modelling domain in Figure 2.4 is used for this;

- Also for the Wadden Sea network, we compare our time-dependent friction simulations with Reef et al.'s steady friction model;
- The additional processes captured by the time-dependent friction model are difficult to investigate with the comprehensive Wadden Sea network. Therefore, we perform simulations with idealized single channels forced by tide, wind and both (Figure 2.2);
- The simultaneous forcing and time-dependent friction coefficient allows for tide-surge interaction and offers with that new insights for idealized modelling.

The simulation results for the single channel system and the Wadden Sea network are given in **chapter 4** and **chapter 5**, respectively.

The above mentioned chapters provide the necessary information to answer the research questions, which is subsequently discussed and answered in respectively **chapter 6** and **chapter 7**.

# Chapter 2

## Model formulation

The model formulation is described in the following sections. Firstly, section 2.1 discusses the general network geometry and how it is applied to our simulation cases. The model presented in this study should be applicable to any shallow water system with predominantly one-dimensional flow. This is for us the tidal channel system of the Dutch Wadden Sea. However, it could also be a fjordic channel network, which was for instance modelled by Hill and Souza (2006). Secondly, section 2.2 discusses the hydrodynamics, that is the governing equations, the forcing and the boundary conditions. Section 2.3 discusses the description of our time-dependent friction coefficient  $r_j(t)$ .

### 2.1 Network geometry

The simulation cases are translated to a network of one-dimensional flow channels. This subsection describes first the general network geometry, secondly the single channel case and then the Wadden Sea.

#### General network geometry

Figure 2.1 provides an example of a typical network with all key features of tidal networks. The tidal channels are considered straight and are on both ends connected to a node. There are three types of nodes.

1. Closed boundary nodes are indicated by bars.
2. Internal nodes that are indicated by solid circles. This type connects two or more channels with each their own dimensions.
3. Open boundary nodes are indicated by open circles. This type connects the open sea with a tidal channel and forces the system by imposing the sea surface elevation as a boundary condition.

Tidal channels are numbered and nodes are named by capitalized letters. Each channel is dimensionalized with a depth  $h_j$ , width  $b_j$  and length  $L_j$ , where subscript  $j$  indicates the channel number. To mimic the non-rectangular tidal channel bathymetry more closely, we allow for multiple rectangular channels that are parallel aligned and originate and terminate in the same nodes. The channels are given a specific direction (see arrow). Note that this is *not* the flow direction – which changes during ebb and flood –, it is necessary for the coordinate direction (see section 2.2). The channel angle with respect to north is given by  $\beta_j$ . This angle is in degrees and increases in clockwise direction. The entire system is forced by a spatially uniform wind stress which is projected on each channel. The time-dependent wind angle is given by  $\alpha(t)$ . This angle is also in degrees and increases also in clockwise direction.

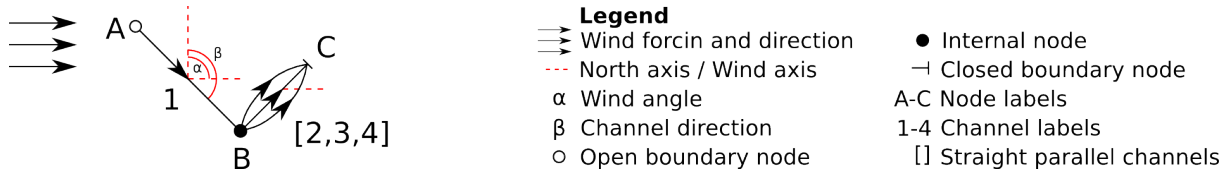


Figure 2.1: An example network forced by both tide and wind.

### Single channel

We investigate three single channel subcases, see Figure 2.2, forced by (a) wind, (b) tide and (c) both. The channel length is 100 kilometres and the depth is 4 metres. The synthetic forcing signals are depicted in Figures 2.3.

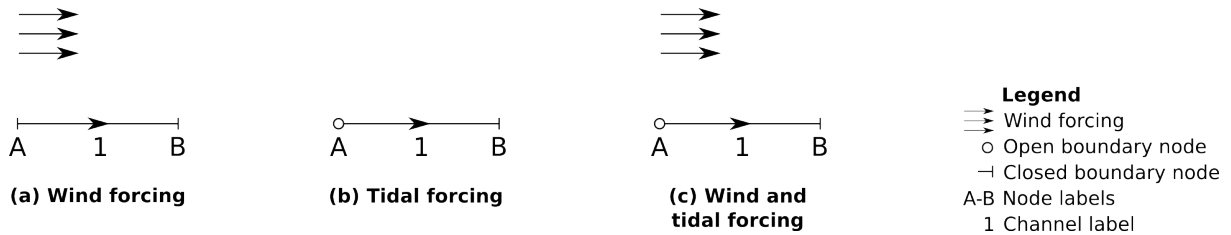


Figure 2.2: A single channel forced by (a) wind, (b) tide and (c) both. Note that an open boundary node can be forced by both tide and wind, henceforth, it is named open boundary forcing.

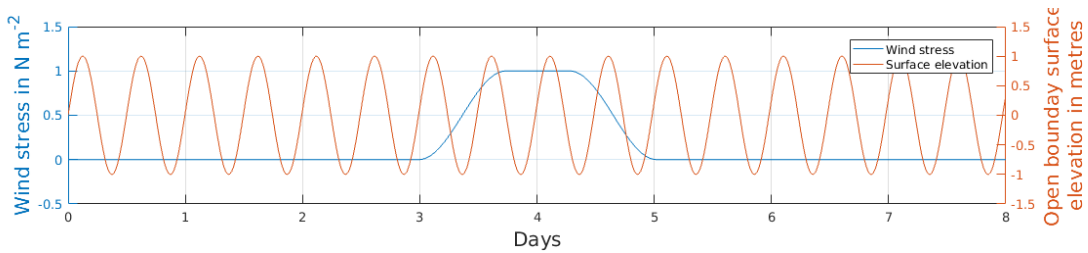


Figure 2.3: The single channel forcing signals for both the open boundary elevation and wind stress.

### Wadden Sea network

The State Committee (1926) applied two different Wadden Sea networks. A tidal channel network for forcing conditions dominated by tide and a storm network to accommodate the larger discharges during storms. Reef et al. (2016) applied the same networks. We proceed with the storm network since our main interest is in storm conditions. This network is depicted in Figure 2.4.

The channel-dependent information is provided in Table 2.1. Rijkswaterstaat (2017) provides measurement data for sea surface elevations. There are three measurement stations near the tidal inlets, that is Den Helder near the Marsdiep-inlet, Vlieland haven near the Vlie-inlet and Wierumergronden near the Pinkegat-inlet. There are also three measurement stations inside the back-barrier bay, that is Den Oever near node D, Kornwerderzand near node E and Harlingen between nodes E, F and K. The sea surface elevations for the 2013 Sinterklaasstorm are plotted in Figures 2.5 and 2.6.

KNMI (2017) provides wind measurements for several locations in and around the Wadden Sea. Figure 2.7 depicts the wind stress and direction for the measurement station on the Vlieland barrier island.

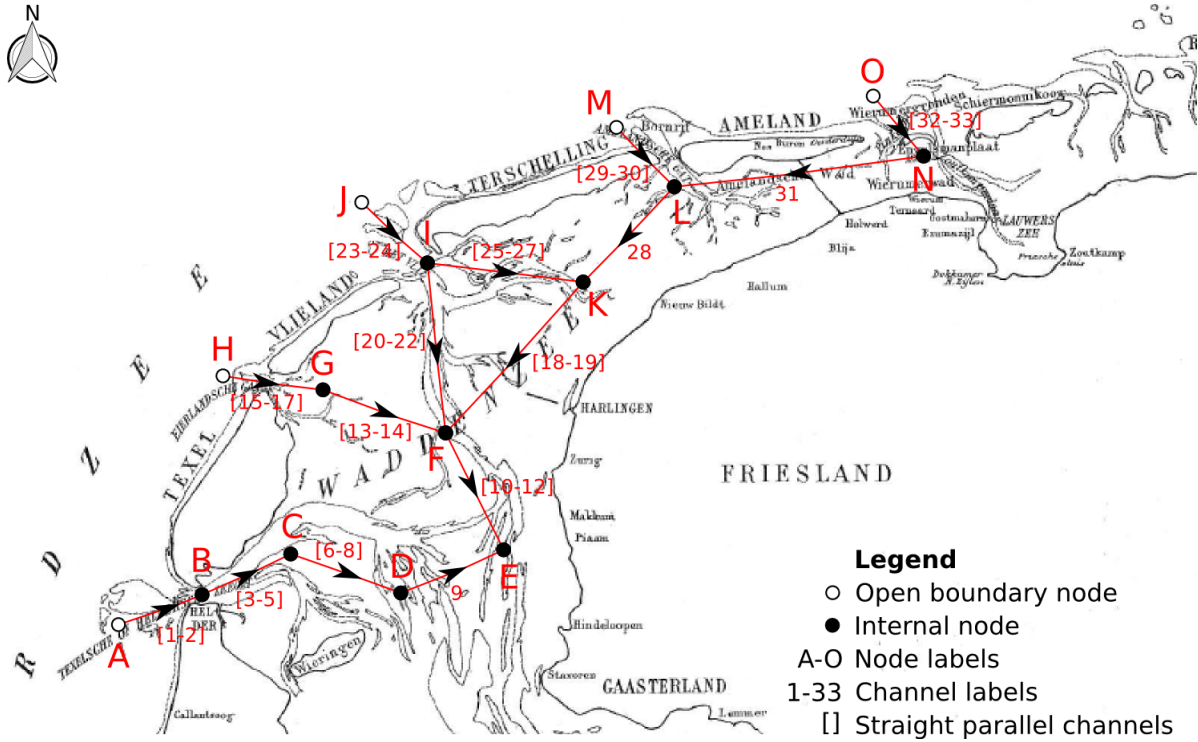


Figure 2.4: The Wadden Sea tidal channel network setup. The underlying map displays the nineteenth century Dutch Wadden Sea. This map, and the network setup, are obtained from the State Committee (1926). The closure dam the Afsluitdijk is not displayed on this map. The time-dependent wind angle of the 2013 Sinterklaasstorm is not indicated on this figure. The tidal channels and labels have been highlighted red to stand out.

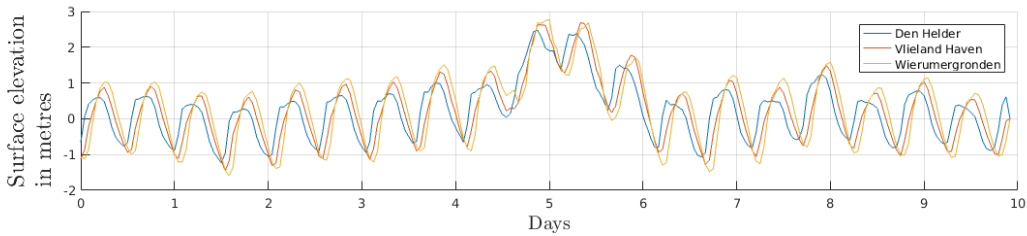


Figure 2.5: Surface elevations with respect to N.A.P. at measurements stations Den Helder, Vlieland Haven and Wierumergronden during the 2013 Sinterklaasstorm. First measurement is at December 1th 01:00 local time. The hourly values are 10 minute averages over the previous and next 5 minutes at the stroke of the clock.

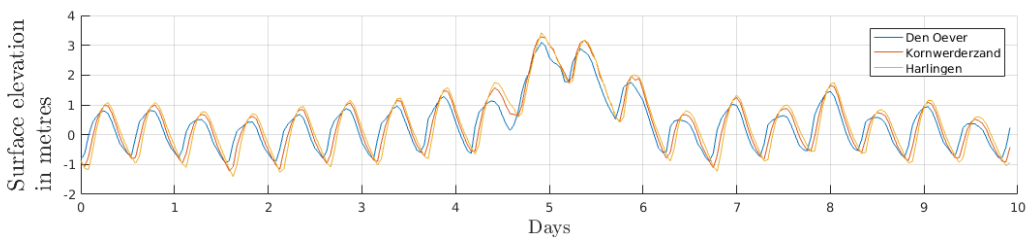


Figure 2.6: Surface elevations with respect to N.A.P. at measurements stations Den Oever, Kornwerderzand and Harlingen during the 2013 Sinterklaasstorm. First measurement is at December 1th 01:00 local time. The hourly values are 10 minute averages over the previous and next 5 minutes at the stroke of the clock.

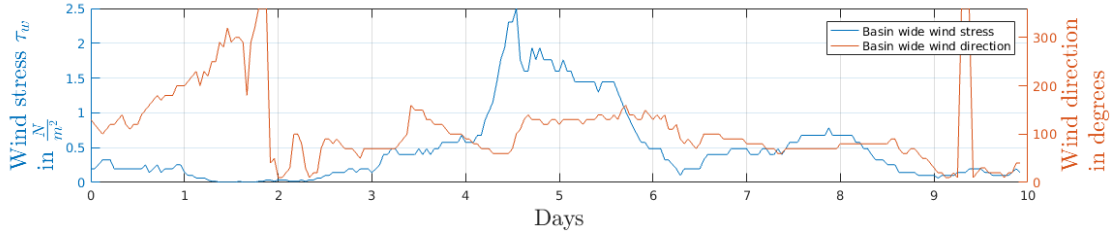


Figure 2.7: The wind stress and direction at measurement station Vlieland during the 2013 Sinterklaasstorm. The first measurement is at December 1st 01:00 local time. Note that the wind direction is actually measured and that the wind stress is calculated from wind speed measurements, see equation (2.1). The wind speed values are hourly averages. The hourly wind direction values are 10 minute averages of the previous 10 minutes before the stroke of the clock. The wind direction is 360, 270, 180 and 90 degrees for respectively north, west, south and east. Data obtained from KNMI (2017).

## 2.2 Hydrodynamics

Each channel  $j$  is described by the linearized one-dimensional shallow water equations. Assuming that the surface elevation with respect to the undisturbed water level is much smaller than the mean depth, that is  $\zeta_j \ll h_j$ , the cross-sectionally-averaged shallow water equations are expressed in linearized form by

$$\begin{aligned} \frac{\partial u_j}{\partial t} + \frac{\tau_{b,j}}{\rho h_j} + g \frac{\partial \zeta_j}{\partial x_j} &= \frac{\tau_{w,j}}{\rho h_j}, \\ \frac{\partial \zeta_j}{\partial t} + h_j \frac{\partial u_j}{\partial x_j} &= 0, \end{aligned}$$

with cross-sectionally averaged velocity  $u_j$ , along-channel coordinate  $x_j$  and time  $t$ . Unless explicitly mentioned otherwise, when we discuss the velocity, we mean the cross-sectionally averaged velocity. The surface elevation  $\zeta_j$  is with respect to the undisturbed water level. The gravitational acceleration  $g$  and water density  $\rho$  are steady and spatially uniform throughout the basin. These parameters are provided in Table 2.2. Channel dependent parameter  $h_j$  is the mean water depth and is provided in Table 2.1, along with length  $L_j$ , width  $b_j$  and direction  $\beta_j$ . These parameters are time-independent and spatially uniform within the channel. The linearized bottom stress  $\tau_{b,j}$  is described with a time-dependent friction coefficient  $r_j(t)$  and is further discussed in section 2.3. The steady friction coefficients  $r_j$  – for the performance comparison of  $r_j(t)$  – are described at the end of this section. The along-channel and time-periodic wind stress  $\tau_{w,j}$  is provided in Figure 2.3 for the single channel case. The channel dependent wind stress signals for the Wadden Sea network result from the wind measurements in Figure 2.7<sup>1</sup>. These measurements provide the time-dependent direction  $\alpha(t)$  and wind speed  $u_w(t)$ , which are assumed spatially uniform within the back-barrier bay. The projected wind stress  $\tau_{w,j}$  on channel  $j$  is calculated with

$$\tau_{w,j}(t) = \tau_w(t) \cos(\beta_j - \alpha(t)).$$

An example of wind direction  $\alpha$  and channel direction  $\beta_j$  is given in Figure 2.1. The time-dependent wind stress  $\tau_w(t)$  is – as suggested by Pugh (1987) – calculated with

$$\tau_w(t) = c_w \rho_a u_w^2, \quad (2.1)$$

<sup>1</sup> The wind measurements in Figure 2.7 are obtained on the barrier island Vlieland. There are several measurement stations in and around the Wadden Sea. However, these measurements are at varying altitudes and therefore require different values of  $c_w$ . Since we are comparing our model results with Reef et al. (2016), we have chosen to also assume the Vlieland measurements as spatially uniform throughout the basin. Note however that the wind forcing could be better approximated.

where  $c_w$  is the dimensionless wind drag coefficient and  $\rho_a$  the air density. These parameters are provided in Table 2.2.

With the inclusion of friction and the periodic wind forcing, the system tends toward a dynamic equilibrium in which frictional dissipation balances wind power input (Chen et al., 2015)<sup>2</sup>. Henceforth, our model solutions are designed for a dynamic equilibrium and there is no need to consider the initial conditions.

### Boundary conditions and open boundary forcing

There are two boundary conditions per channel, or in terms of nodal requirements, there are four types of nodal requirements.

The kinematic condition states that at closed boundaries the cross-sectionally averaged flow is zero, that is

$$u_j(X_j, t) = 0,$$

with channel end  $X_j$  that is either  $x_j = 0$  or  $x_j = L_j$ .

There are two nodal requirements at each internal node. The first states that the net incoming discharge is equal to zero, that is

$$\sum_{J_C} f_j Q_j = \sum_{J_C} f_j b_j h_j u_j = 0,$$

where  $J_C$  is the set of adjacent channels. Parameter  $f_j$  is +1 for an incoming channel direction and  $-1$  for an outgoing channel direction (see Figure 2.1).  $Q_j$  is the channel discharge. The second requirement states that the surface elevation must be equal at all channel ends. Let  $J_C$  be the set of channels 1, 2 and 3 with channel ends  $L_1$ , 0 and  $L_3$ , then there are two conditions, for instance

$$\begin{aligned} \zeta_1(L_1) &= \zeta_2(0), \\ \zeta_2(0) &= \zeta_3(L_3). \end{aligned}$$

The last nodal requirement is at the open boundary. This condition imposes the adjacent sea-surface elevation onto the node, that is

$$\zeta_j(X_j) = \hat{\zeta}_N(t),$$

where  $N$  is the node index. Open boundary forcing can be the astronomical tide, the residual or a combination of both, that is the measured sea-surface elevation. The residual consists of the elevation due to surge and tide-surge interaction. The measured sea-surface elevations are given in Figure 2.5. The synthetic forcing signal for the single channel case is given in Figure 2.3.

## 2.3 Time-dependent friction coefficient $r_j(t)$

The bottom friction parametrization  $\tau_{b,j}$  is usually quadratic, which we replace by a parametrization that includes a linearly applied friction coefficient  $r_j(t)$ , that is

$$\begin{aligned} \tau_{b,j}(t) &= \overbrace{c_{d,j} \rho |u_j| u_j}^{\text{quadratic}} = \overbrace{r_j(t) \rho u_j}^{\text{linearly applied}}, \\ \text{with } c_{d,j} &= \frac{g M_n^2}{h_j^{1/3}}. \end{aligned} \tag{2.2}$$

---

<sup>2</sup>Without friction, pure resonance may result in a net input of energy by the wind forcing leading to ever-increasing oscillations.

Here,  $c_{d,j}$  is the dimensionless drag coefficient and  $M_n$  is the Manning roughness coefficient. The latter is taken equal to Reef et al. (2016)<sup>3</sup> and is provided in Table 2.2. The cross-sectionally averaged velocity  $u_j$  varies both in time and space and the bottom friction coefficient  $r_j(t)$  is allowed to vary in time but *not* in space. Note that the nonlinear  $c_{d,j}|u_j|u_j$  is replaced by the essentially nonlinear  $r_j(t)u_j$ , both parametrizations have products of unknowns. However, the bottom friction coefficient  $r_j(t)$  will be determined through iterations and subsequently described by a Fourier transformation to enable linear calculations. This will be discussed further in chapter 3. The time-dependency allows us to capture the nonlinear variation in bottom stress over the various stages of the storm event:  $r_j(t)$  will be large whenever the flow is strong and small when it is weak.

To specify the friction coefficient, we adopt an energy argument analogous to that of Lorentz (1922), but now in an instantaneous rather than tidally averaged sense. Specifically,  $r_j(t)$  must be such that the instantaneous frictional energy dissipation integrated over the channel is identical for both parametrizations in equation (2.2):

$$\int_0^{L_j} c_{d,j}\rho|u_j|u_j^2 dx = \int_0^{L_j} r_j(t)\rho u_j^2 dx.$$

This balance results in the linearization criterion for the time-dependent friction coefficient:

$$r_j(t) = c_{d,j} \frac{\int_0^{L_j} |u_j|u_j^2 dx}{\int_0^{L_j} u_j^2 dx}. \quad (2.3)$$

Note that both the numerator and denominator can only be positive, henceforth,  $r_j(t)$  is positive throughout time. We make two remarks:

- Just as the steady friction coefficient  $r_j$ , specifying  $r_j(t)$  requires knowledge of the flow solution  $u_j(x_j, t)$ , which in turn depends on  $r_j(t)$ . This fundamental difficulty is tackled by adopting an iterative procedure that seeks to improve this first guess. This is further described in section 3.4.
- The linear friction coefficient  $r_j(t)$  depends on  $t$  but not on  $x_j$ . It is thus meant to represent the channel as a whole, which remains an important simplification compared to the original quadratic parametrization in equation (2.2).

Considering the latter remark and supposing a sinusoidally varying velocity  $u_j(x_j, t^*)$  throughout the channel and  $r_j(t^*)$  at the instantaneous moment  $t = t^*$ , then the quadratic bottom friction is constantly under- or overestimated throughout the channel. Overestimating results in an overestimated delay<sup>4</sup> of the progressing current whereas underestimating has the reverse effect. Analogously, overestimation results in overdamping of the velocity.

The temporal profile of  $r_j(t)$  is obtained with Matlab.

### Simulations with steady friction coefficient

In these first simulations, we compare our Wadden Sea network results with the earlier results by Reef et al. (2016). We therefore apply the same friction coefficient as Reef et al., that is  $r_j$  in equation (1.1).

The single channel simulations are more focused on how much  $r_j(t)$  includes the physical processes. We choose therefore a steady friction coefficient that represents the energy dissipation

<sup>3</sup>Reef et al. cites Chow (1959) on the Manning coefficient. It should however be noted that roughness coefficients are empirical and uncertain. For example the range of the Manning coefficient given by Chow for major natural streams (larger than 100 feet width) is from 0.025 to 0.060.

<sup>4</sup>Friction holds the flow back (delays).

better. We specify  $r_j$  in this case by equalling the linearized energy dissipation throughout time and space to the quadratic energy dissipation, that is

$$r_j \int_0^{T_{recur}} \int_0^{L_j} u_j^2 dx dt = c_{d,j} \int_0^{T_{recur}} \int_0^{L_j} |u_j| u_j^2 dx dt,$$

which results in the linearized friction coefficient

$$r_j = c_{d,j} \frac{\int_0^{T_{recur}} \int_0^{L_j} |u_j| u_j^2 dx dt}{\int_0^{T_{recur}} \int_0^{L_j} u_j^2 dx dt}, \quad (2.4)$$

that is uniform in time and space.  $T_{recur}$  is the storm duration. By ensuring that the total linearized energy dissipation is equal to the quadratic version, we assist the comparison with the energy dissipation by the time-dependent friction coefficient  $r_j(t)$ .

Table 2.1: The values of the channel-dependent parameters for the Wadden Sea network in Figure 2.4. Source: the State Committee (1926) and Reef et al. (2016).

Nodal connection $N$	Channel number $j$	Mean depth $h$ $m$	Mean width $b$ $km$	Length $L$ $km$	Direction $\beta$ $degrees$
AB	1	9	8	10	67.4
	2	20	2		
BC	3	27	2	13	67.4
	4	15	2		
	5	8	2		
CD	6	4	20.5	15	135
	7	20	1.5		
	8	10	1		
DE	9	6	12	16	69.8
EF	10	6	9	17	166
	11	16	1.5		
	12	4	10.5		
FG	13	3.5	14	12	104
	14	8	2		
HG	15	10	1.5	8.5	104
	16	6	2.5		
	17	1	4		
FK	18	6.5	4	16	206
	19	3.5	6		
FI	20	18	1.3	19	159.9
	21	4	9.7		
	22	9	2		
IJ	23	9	11	9	135
	24	18	2		
IK	25	16	1	14	93.8
	26	9	2		
	27	4	5		
KL	28	5	16	13	239.3
LM	29	21	1.2	14	135
	30	5	3.8		
LN	31	5.5	8.5	19	268.9
NO	32	5	11	13	143.1
	33	12	1.5		

Table 2.2: Parameter values that are steady and spatially uniform throughout the basin.

Description	Sym.	Value	Units	Source
Air density	$\rho_a$	1.225	$kg\ m^{-3}$	Pugh (1987)
Gravitational acceleration	$g$	9.81	$m\ s^{-2}$	
Manning coefficient	$M_n$	0.03	$s\ m^{-1/3}$	Chow (1959)
Sea water density	$\rho$	1025	$kg\ m^{-3}$	
Wind drag coefficient	$c_w$	0.0033	–	State Committee (1926)

# Chapter 3

## Solution method

This chapter implements our time-dependent friction coefficient in a linear fashion. Using the Discrete Fourier Transformation, we first express the non-linear behaviour of the forcing and friction in the frequency domain (subsection 3.1.1). This spectral approach results in a Helmholtz-type differential problem per frequency which is coupled to other frequencies (subsections 3.1.2 and 3.1.3). Section 3.2 expresses the problem in matrix notation and diagonalizes the problem to a Helmholtz-problem, for which a solution is familiar. The problem is then solved in section 3.3 using linear algebra. Our friction coefficient is dependent on the the cross-sectionally averaged velocity solution, which in turn is dependent on the friction coefficient. The iterative process adopted to address this difficulty is discussed in section 3.4.

### 3.1 Spectral approach

#### 3.1.1 Fourier representation

We decompose the friction coefficient  $r_j(t)$  and forcing signals into continuous sinusoidal signals in the frequency domain, such that the superposition of these continuous signals is equal to the original signals. For this we apply the Discrete Fourier Transformation. These simple sinusoidal signals allow us to apply the non-linear behaviour in a linear solution method. Reef et al. (2016) applied the same technique and based this on Chen et al. (2015) and Chen et al. (2016). We obtain a solution for each frequency since the model input is in the frequency domain. The full solution is the superposition of all frequencies.

All Fourier series are given by

$$\begin{pmatrix} r_j(t) \\ \hat{\zeta}_N(t) \\ \tau_{w,j}(t) \\ u_j(x_j, t) \\ \zeta_j(x_j, t) \end{pmatrix} = \sum_{m=-M}^M \begin{pmatrix} R_{j,m} \\ H_{N,m} \\ \mathcal{T}_{j,m} \\ U_{j,m}(x_j) \\ Z_{j,m}(x_j) \end{pmatrix} \exp i\omega_m t, \quad (3.1)$$
$$\omega_m = m \frac{2\pi}{T_{recur}} = m\omega_{min},$$

where complex amplitudes  $R_{j,m}$ ,  $H_{N,m}$ ,  $\mathcal{T}_{j,m}$ ,  $U_{j,m}$  and  $Z_{j,m}$  are for the positive modes  $m$  the complex conjugates of negative modes  $-m$ . This is necessary since the in- and output are real-valued. The Fourier signals are strictly speaking recurring sinuses and we can therefore consider the forcing duration  $T_{recur}$  to be the fictitious recurrence period of the storm event. Associated with this is the minimum frequency  $\omega_{min}$ . The truncation number  $M$  results firstly from the number of measurements of the forcing input, that is the temporal resolution. A small resolution results in a small truncation number. Since we are considering analytical solutions, note that the output in-between measurements is solely based on the temporal interpolation to

continuous signals in the Fourier expansion. Secondly, the computational burden can be reduced by lowering the truncation number, this in turn results in loss of representation. As example is in Figure 3.1 the Fourier domain and the reconstructed wind stress profile for the single channel case given.

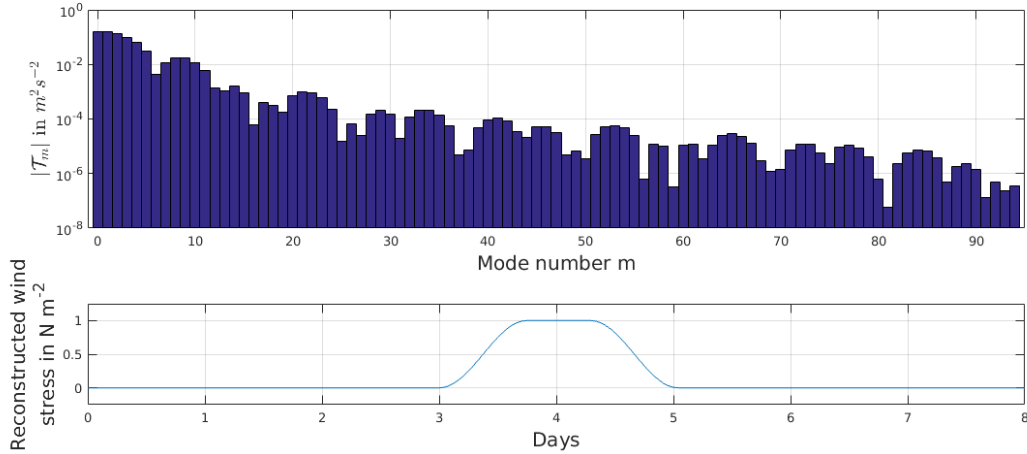


Figure 3.1: The Fourier domain (top) and the reconstructed wind stress (bottom) of the single channel case (see Figure 2.3). The frequency  $\omega_m$  is given by equation (3.1) and truncation number  $M = 95$  and recurrence period  $T_{recur} = 8$  days.

### 3.1.2 Convolution sum

Reef et al. (2016) found the differential problem to the complex amplitudes  $U_{j,m}(x_j)$  and  $Z_{j,m}(x_j)$  by first substituting the Fourier series into the shallow water equations and boundary conditions and then dividing out the exponential term. Since only the exponential term is dependent on time  $t$ ,  $U_{j,m}$  and  $Z_{j,m}$  are solely dependent on the along-channel coordinate  $x_j$ .

We apply – in contrast to Reef et al.’s steady  $r_j$  – the friction coefficient as a Fourier series, and with that, have a product of two Fourier series in the frictional term of the momentum equation. This results in unequal frequencies per term and prevents us from dividing out all time-dependencies. If we would want to continue using Reef et al.’s method and exclude the double frequency, we could only use the zero mode of the frictional Fourier series for each mode  $m$ . However, this would mean that we are – again – applying a steady friction coefficient.

Choosing an appropriate frictional mode in combination with the mode  $m$ -dependent differential problem leads in fact to our new implementation method in which we must apply a convolution sum. In this convolution sum we superpose all combinations of the frictional and velocity modes that are combined the  $m^{\text{th}}$  frequency. The frictional term in the momentum equation then becomes for the  $m^{\text{th}}$  frequency

$$\frac{1}{h_j} \left\{ r_j(t) u_j \right\}_m = \frac{1}{h_j} \left\{ \begin{array}{l} R_{j,m-M} \exp i\omega_{m-M} t \times U_{j,M} \exp i\omega_M t \\ \vdots \\ R_{j,0} \exp i\omega_0 t \times U_{j,m} \exp i\omega_m t \\ \vdots \\ R_{j,m} \exp i\omega_m t \times U_{j,0} \exp i\omega_0 t \\ \vdots \\ R_{j,M} \exp i\omega_M t \times U_{j,m-M} \exp i\omega_{m-M} t \end{array} \right\}_m, \quad (3.2)$$

$$= \frac{1}{h_j} \left\{ \sum_n R_{j,m-n} U_{j,n} \exp i\omega_m t \right\}_m,$$

with the convolution sum between the curly brackets and appropriate ranges for  $n$  such that indices  $n$  and  $m - n$  do not outrange  $\pm M$ . Section 3.2 provides more clarity on these ranges.

### 3.1.3 Differential problem for $Z_{j,m}(x_j)$

We express our problem in terms of  $Z_{j,m}(x_j)$  and eventually find the solution to the velocity amplitude  $U_{j,m}(x_j)$  through the momentum equation, which is discussed in section 3.2. The differential problem for  $Z_{j,m}(x_j)$  is found by substituting the convolution sum and Fourier series into the shallow water equations and boundary conditions.

The shallow water equations can then be expressed in one single differential equation by substituting the conservation of mass into the spatial derivative of the momentum equation, that is

$$Z_{j,m}'' = \frac{i^2 \omega_m^2}{gh_j} Z_{j,m} + \frac{1}{gh_j^2} \left[ \sum_n R_{j,m-n} i\omega_n Z_{j,n} \right]. \quad (3.3)$$

The result is a coupled Helmholtz-type boundary value problem in terms of  $Z_{j,m}$  and  $Z_{j,n}$  only.

The boundary conditions transform towards

$$\begin{aligned} U_{j,m}(X_j) &= 0, \\ Z_{j,m}(X_j) &= Z_{j+1,m}(X_{j+1}), \\ \sum_{J_C} f_j b_j h_j U_{j,m}(X_j) &= 0, \\ Z_{j,m}(X_j) &= H_{N,m}, \end{aligned}$$

Note that the elevation condition considers channel  $j + 1$  to be connected to channel  $j$ . This is an example and does not reflect the Wadden Sea geometry. Section 3.2 expresses the boundary conditions in terms of  $Z_{j,m}(x_j)$  only. We use a simpler matrix notation for this.

## 3.2 Decoupling problem

This section decouples the coupled Helmholtz-type problem to a Helmholtz problem, a problem for which the solution is familiar and solved in section 3.3. The differential problem is first written in a matrix notation and then diagonalized to a decoupled Helmholtz problem.

### Matrix notation

The boundary value problem of equation (3.3) is given in matrix notation by

$$\mathbf{z}_j'' = \frac{1}{gh_j} \left[ \mathbf{D} + \frac{1}{h_j} \mathbf{R}_j \right] \mathbf{Dz}_j = \frac{1}{gh_j} \mathbf{V}_j \mathbf{Dz}_j = \mathbf{B}_j \mathbf{z}_j. \quad (3.4)$$

where  $\mathbf{z}_j = (Z_{j,-M} \ \cdots \ Z_{j,0} \ \cdots \ Z_{j,M})^T$ ,

$$\mathbf{D} = \text{diagonal}(i\omega_{-M} \ \cdots \ i\omega_{-1} \ 0 \ i\omega_1 \ \cdots \ i\omega_M),$$

$$\text{and } \mathbf{R}_j = \begin{pmatrix} R_{j,0} & \cdots & R_{j,-M} & 0 & 0 \\ \vdots & R_{j,0} & \cdots & R_{j,-M} & 0 \\ R_{j,M} & \vdots & R_{j,0} & \cdots & R_{j,-M} \\ 0 & R_{j,M} & \vdots & R_{j,0} & \vdots \\ 0 & 0 & R_{j,M} & \cdots & R_{j,0} \end{pmatrix}.$$

Diagonal matrix  $\mathbf{D}$  is the time-derivative matrix with entries  $im\omega_{min}$ . Henceforth, the middle entry is zero since the middle mode is also zero. The frictional convolution matrix  $\mathbf{R}_j$  is a Toeplitz matrix; the elements in the descending diagonals are constant. The friction matrix consists of values  $R_{m-n}$  with per column increasing  $n$  and per row increasing  $m$ . Both  $n$  and  $m$  increase from  $-M$  to zero to  $M$ . The values  $R_{m-n}$  are the complex amplitudes that resulted from the Fourier transformation of the time-dependent friction coefficient, see equation (3.1). Hence, the values of  $R_{m-n}$  with  $|m-n| > M$ , are zero. Matrix  $\mathbf{V}_j$  is necessary for the boundary conditions and finding the velocity solution. Provided  $r_j(t)$  is time-dependent, the friction matrix  $\mathbf{R}_j$  makes matrix  $\mathbf{B}_j$  non-diagonal and thus the problem coupled.

The boundary conditions are preferably in terms of  $Z_{j,m}$  only, this can be achieved by substituting the momentum equation into the closed boundary condition and the equal flow condition. The momentum equation is given in matrix notation by

$$\mathbf{D}\mathbf{u}_j + \frac{1}{h_j}\mathbf{R}_j\mathbf{u}_j + g\mathbf{z}'_j = \frac{1}{\rho h_j}\mathbf{t}_j,$$

where  $\mathbf{u}_j = (U_{j,-M} \ \cdots \ U_{j,0} \ \cdots \ U_{j,M})^T$ ,

and  $\mathbf{t}_j = (\mathcal{T}_{j,-M} \ \cdots \ \mathcal{T}_{j,0} \ \cdots \ \mathcal{T}_{j,M})^T$ .

The vectors  $\mathbf{u}_j$  and  $\mathbf{t}_j$  contain the Fourier amplitudes of the velocity and the wind forcing. The boundary conditions – the closed boundary condition, equal elevation condition, equal flow condition and open boundary condition respectively – are then given by

$$g\mathbf{V}_j^{-1}\mathbf{z}'_j(X_j) = \frac{1}{\rho h_j}\mathbf{V}_j^{-1}\mathbf{t}_j,$$

$$\mathbf{z}_j(X_j) = \mathbf{z}_{j+1}(X_{j+1}),$$

$$\sum_{J_C} f_j b_j h_j g \mathbf{V}_j^{-1} \mathbf{z}'_j(X_j) = \sum_{J_C} \frac{f_j b_j h_j}{\rho} \mathbf{V}_j^{-1} \mathbf{t}_j,$$

$$\mathbf{z}_j(X_j) = \mathbf{H}_{N,m}.$$

### Diagonalizing the problem

Would  $\mathbf{B}_j$  have been a diagonal matrix, then the boundary value problem in equation (3.4) would have been a Helmholtz problem.

Boas (2006) shows in section 3.11, and specifically equation (11.11) of that section, that matrix  $\mathbf{B}_j$  can be transformed to diagonal matrix  $\mathbf{Q}_j$  with the eigenvector matrix of  $\mathbf{B}_j$ , that is

$$\mathbf{P}_j^{-1}\mathbf{B}_j\mathbf{P}_j = \mathbf{Q}_j,$$

where  $\mathbf{P}_j$  is the right-hand eigenvector matrix.

Substituting the above expression into the boundary value problem results in a Helmholtz problem as given by

$$\mathbf{P}_j^{-1}\mathbf{z}''_j = \mathbf{Q}_j\mathbf{P}_j^{-1}\mathbf{z}_j \quad \text{or relabelled as} \quad \mathbf{y}''_j = \mathbf{Q}_j\mathbf{y}_j.$$

Vector  $\mathbf{y}_j$  has entries  $Y_{j,n}$  where index  $n$  goes from  $-M$  to zero to  $M$ . The entries of diagonal matrix  $\mathbf{Q}_j$  are the eigenvalues  $\lambda_{j,n}$  of matrix  $\mathbf{B}_j$  (in arbitrary order), or written with wave numbers  $\mu_{j,n}$  as entries  $-\mu_{j,n}^2$ . Since matrix  $\mathbf{B}_j$  has a zero column, we know that there is also

a zero eigenvalue<sup>1</sup>. By using  $\mathbf{P}_j^{-1}\mathbf{z}_j = \mathbf{y}_j$ , we can express the complex amplitude solutions and boundary conditions in terms of  $Y_{j,n}$  only, that is

$$\begin{aligned}\mathbf{z}_j &= \mathbf{P}_j\mathbf{y}_j, \\ \mathbf{u}_j &= \mathbf{V}_j^{-1}\left[\frac{1}{\rho h_j}\mathbf{t}_j - g\mathbf{P}_j\mathbf{y}'_j\right], \\ \mathbf{y}'_j(X_j) &= \frac{1}{\rho g h_j}\mathbf{P}_j^{-1}\mathbf{t}_j, \\ \mathbf{P}_j\mathbf{y}_j(X_j) &= \mathbf{P}_{j+1}\mathbf{y}_{j+1}(X_{j+1}), \\ \sum_{\mathcal{J}_C} f_j b_j h_j g \mathbf{V}_j^{-1} \mathbf{P}_j \mathbf{y}'_j(X_j) &= \sum_{\mathcal{J}_C} \frac{f_j b_j h_j}{\rho} \mathbf{V}_j^{-1} \mathbf{t}_j, \\ \mathbf{y}_j(X_j) &= \mathbf{P}_j^{-1} \mathbf{H}_{N,m}.\end{aligned}$$

Note that the elevation condition considers channel  $j + 1$  to be connected to channel  $j$ . This is an example and does not reflect the Wadden Sea geometry.

### 3.3 Solving problem

The solution to our Helmholtz problem in terms of  $Y_{j,n}$  and wave number  $\mu_{j,n}$  is given by

$$Y_{j,n}(x_j) = \begin{cases} A_{j,n} \cos \mu_{j,n} x_j & + B_{j,n} \sin \mu_{j,n} x_j & \text{if } \mu_{j,n} \neq 0, \\ A_{j,n} x_j & + B_{j,n} & \text{if } \mu_{j,n} = 0, \end{cases}$$

where  $A_{j,n}$  and  $B_{j,n}$  are the integration constants. Notice that there are a total of  $2(2M + 1)$  unknown integration constants per channel  $j$ . We need the same number of boundary conditions, which we indeed have.

The integration constants are found by substituting the solution of  $Y_{j,n}$  into the boundary conditions and concatenating all conditions into one matrix equation, that is

$$\mathbf{M}\mathbf{C} = \mathbf{A}, \quad \text{or reordered as} \quad \mathbf{C} = \mathbf{M}^{-1}\mathbf{A}, \quad (3.5)$$

where each row consists of one condition, matrix  $\mathbf{M}$  consists of all terms dependent of the integration constants, vector  $\mathbf{C}$  consists of all integration constants and vector  $\mathbf{A}$  consists of all terms independent of the integration constants.

Note that the expression above consists of all conditions for each channel  $j$ . Since the equal elevation and equal flow conditions are coupled among all modes  $n$ , equation (3.5) consists of the conditions for each mode and especially matrix  $\mathbf{M}$  can become extremely large. This is in contrast to Reef et al. (2016) who had uncoupled boundary conditions and was therefore able to solve the integration constants per mode. We have provided an example of how matrices  $\mathbf{M}$ ,  $\mathbf{C}$  and  $\mathbf{A}$  are setup in Appendix A, corresponding to the example network in Figure 2.1.

### 3.4 Iteration process

As already noted in section 2.3, the bottom stress depends on the velocity solution, which in turn depends on the bottom stress. This difficulty is solved by adopting an iterative process. The

<sup>1</sup>Eigenvalues can be found by solving  $|\mathbf{B}_j - \lambda_j \mathbf{I}| = 0$  where the vertical bars indicate the determinant and  $\mathbf{I}$  the identity matrix. When evaluating the determinant by using the row containing the  $-\lambda_j$ -element, we notice that all minor determinants – except one – have a zero column and are thus zero. The exception is multiplied by the  $-\lambda_j$ -element and thus has the characteristic polynomial only  $\lambda_j^n$ -terms with integers  $n \geq 1$ . Henceforth, there is an eigenvalue of zero.

iterative procedure is chosen to be under relaxation by averaging the previous friction coefficient with the coefficient resulting from the new velocity profile. Iterations will proceed until the average is equal to the previous friction coefficient. This is when the friction coefficient  $r(t)$  satisfies the linearization criterion in equation (2.3). This process is portrayed in Figure 3.2.

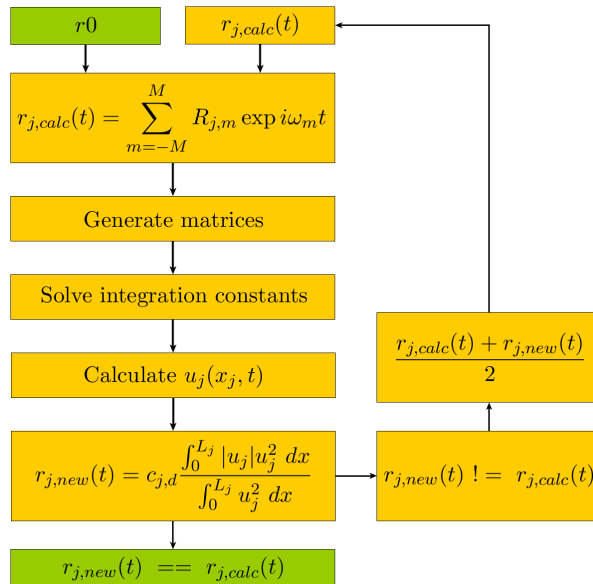


Figure 3.2: The iteration process of the time-dependent friction coefficient  $r(t)$ . In this figure,  $r_0$  is a steady value and the first guess of  $r_j(t)$ ,  $r_{j,new}(t)$  results from the linearization criterion in equation (2.3),  $r_{j,calc}(t)$  is equal to  $r_0$  at the first iteration run and the green boxes indicate either the start or the end of the iteration process. This figure displays the general setup of the model. However, the the model in- and output besides the friction coefficient are not displayed.

# Chapter 4

## Results: Single channel

This chapter presents the simulations for the single channel case. We compare the results with steady and time-dependent friction coefficient for three subcases, that is (a) a closed channel forced by wind only, (b) a channel forced by tide only and (c) a channel forced by both tide and wind. The results are presented in section 4.1. The interaction between tide and surge for case (c) is presented in section 4.2.

The steady friction coefficient is described by the energy based parameter in equation (2.4). This coefficient is a better representation for the quadratic friction (compared to the coefficient by Reef et al. (2016) which overestimates energy dissipation) and with that allows us to highlight the improvements of a time-dependent coefficient. Besides differences in forcing and boundary conditions, is each case the same. The case descriptions are provided in section 2.1, this includes the synthetic forcing signals, channel dimensions and channel setup. Subcase (a) – that is only forced by wind – applies truncation number  $M = 95$ , which is equal to a time step  $\Delta t$  of 1 hour. Simulations involving tide apply a truncation number  $M = 577$  ( $\Delta t = 10$  minutes). The six hour difference between low and high tide (semi-diurnal) requires a larger resolution. The recurrence period  $T_{recur}$  of all subcases is 8 days.

### 4.1 Synthetic forcing

The results for each subcase are presented below the bold highlighted title. We present for each subcase the time-dependent velocity scale (i.e.  $\hat{U}_j(t) = \frac{1}{L_j} \int_0^L |u_j| dx$ ), the steady and time-dependent friction coefficients and the surface elevation at the closed channel end  $x = L$ . The results for the closed channel forced by wind only (subcase a) are given in Figures 4.1 to 4.3. The results for the channel forced by tide only (subcase b) are given Figure 4.4 to 4.6. The results for the channel forced by tide and wind (subcase c) are given Figure 4.7 and 4.8.

#### **(a) Closed channel forced by wind only**

Figure 4.2 shows that the time-dependent friction coefficient follows the time-dependent channel-averaged velocity scale. The steady coefficient exceeds the time-dependent coefficient during peak velocities. This is because the steady coefficient is time- and channel-averaged. The steady friction simulations display critical damping for the surface elevation and slight underdamping for the velocity. The time-dependent friction model displays underdamping when the wind stress has dropped and the elevation attempts to restore to its undisturbed state. This underdamping – which is displayed as sloshing – is visible in both the surface elevation and velocity scale. Underdamping delays the relaxation process significantly such that the fictitious next storm is still influenced by the previous. Underdamping occurs also when the gravitational acceleration and wind stress are in balance; the depth-averaged flow decreases to nearly zero. The overestimated steady friction coefficient slightly delays the increase in velocity at the start of the wind event. The same occurs when the wind stress decreases again.

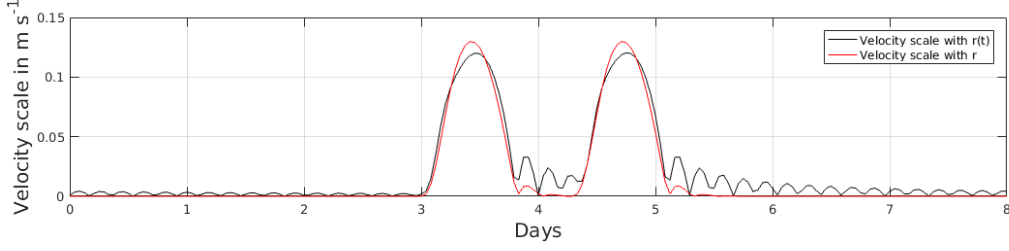


Figure 4.1: The simulated channel-averaged velocity scale for a single channel with closed boundaries and forced by wind. The black and red line are respectively the velocity scale simulated with the time-dependent friction coefficient  $r_j(t)$  and steady coefficient  $r_j$ .

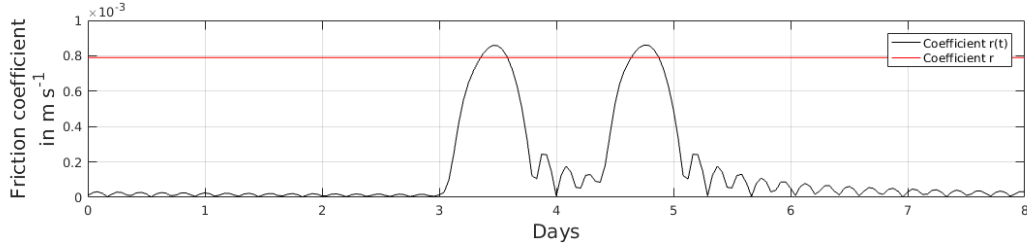


Figure 4.2: The simulated friction coefficients for a single channel with closed boundaries and forced by wind only. The black and red line are the coefficients at the closed boundary  $x = L$  simulated with respectively the time-dependent version  $r_j(t)$  and the steady version  $r_j$ .

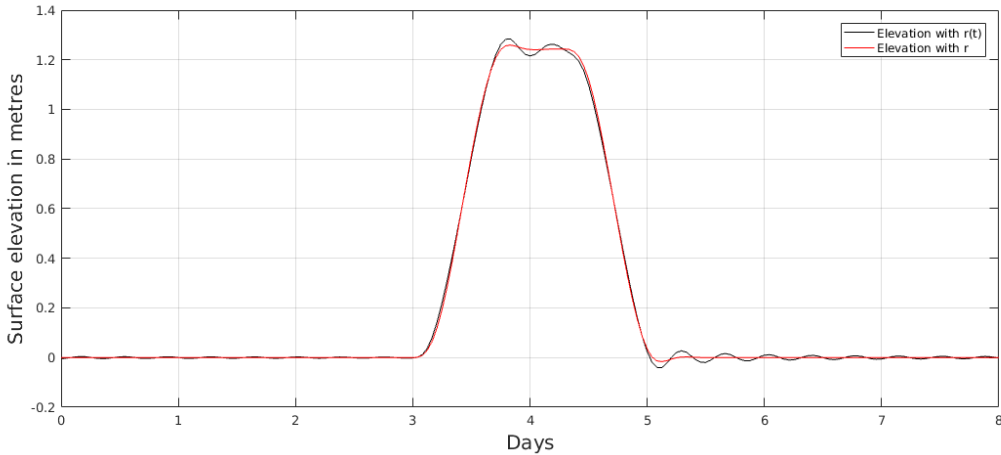


Figure 4.3: The simulated surface elevations for a single channel with closed boundaries and forced by wind. The black and red line are the surface elevations simulated with respectively the time-dependent friction coefficient  $r_j(t)$  and the steady coefficient  $r_j$ .

### (b) Open boundary forced by tide

The elevation profile of the tidal simulations with a steady friction coefficient is more strongly damped and delayed with respect to the time-dependent friction model. The channel-averaged velocity scales and friction coefficients do not decrease to zero and the lowest values do not correspond to high- or low-tide. There is a clear tidal asymmetry visible in both the velocity scale and the friction coefficient. The rising side of the friction coefficient accelerates faster and the velocity scale has a bump on the falling side. The elevation profile does not display (visible) tidal asymmetry. Compared with the simulation of  $r_j(t)$ , the velocity scale profile with  $r_j$  has a smaller maximum value and a larger range.

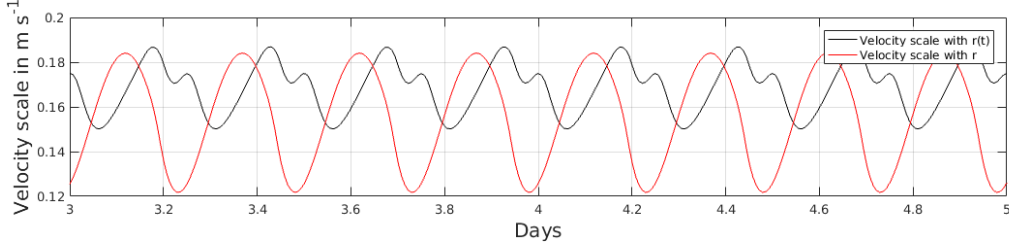


Figure 4.4: The simulated channel-averaged velocity scale for a single channel with an open and closed boundary forced by tide only. The black and red line are respectively the velocity scale simulated with the time-dependent friction coefficient  $r_j(t)$  and steady friction coefficient  $r_j$ . Due to the repetitive tidal pattern we have only plotted day 3 to 5.

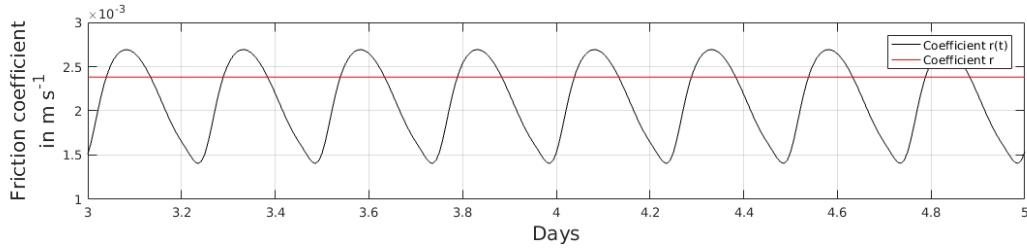


Figure 4.5: The values for the steady (red line) and time-dependent friction (black line) coefficient corresponding to surface elevations in Figure 4.6. Due to the repetitive tidal pattern we have only plotted day 3 to 5.

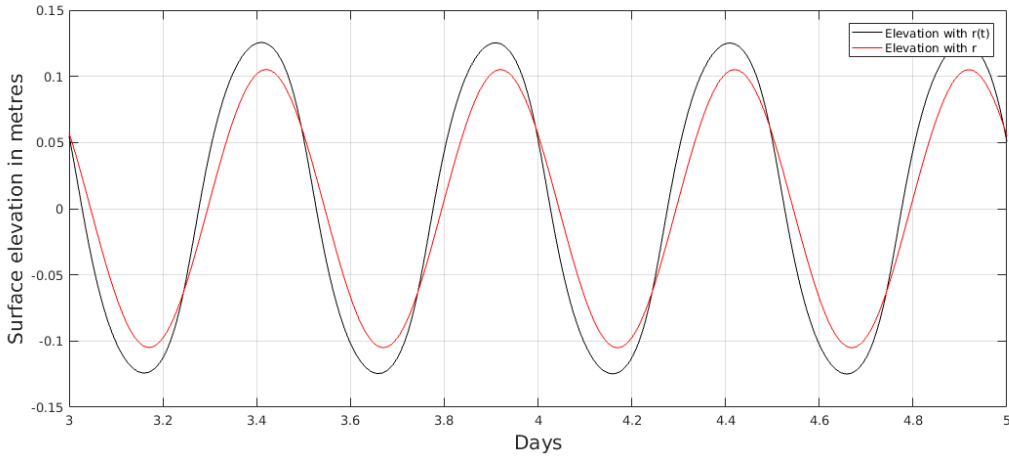


Figure 4.6: Simulated surface elevations for a single channel forced by tide only. The black and red line display the elevations with respectively the steady and time-dependent friction coefficient. Due to the repetitive tidal pattern we have only plotted day 3 to 5.

### (c) Simultaneously forced by tide and wind

The simulations with simultaneous forcing display similar phenomena as for the subcases forced by tide or wind only. For instance, the figures show for simulations with  $r_j$  with respect to  $r_j(t)$  (a) overdamping when flow accelerates, (b) underdamping when flow starts to decelerate and (c) a similar phase shift. Besides that, there is an asymmetry between the ramp-up and ramp-down phase, which is different from the closed channel simulations. This is however not related to the time-dependent friction coefficient but with the change to an open boundary.

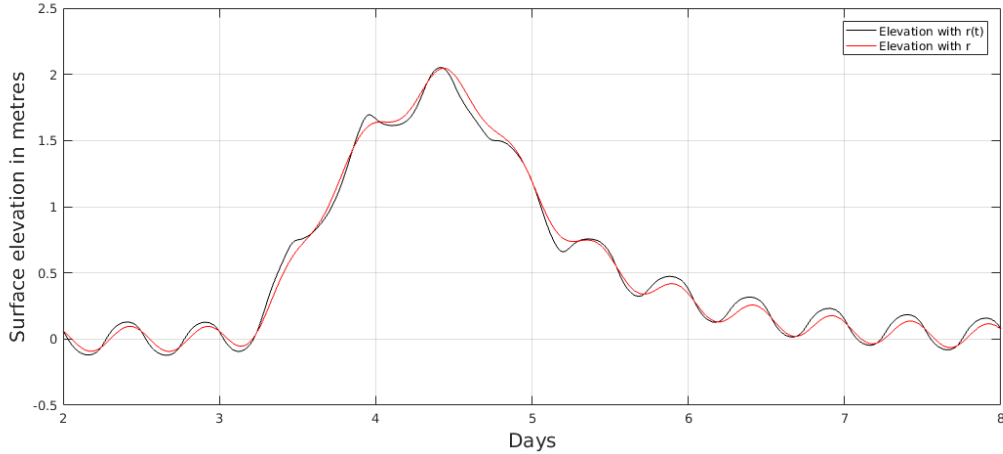


Figure 4.7: Simulated surface elevations for a single channel forced by both tide and wind. The black and red line display the elevations with respectively the steady and time-dependent friction coefficient. The first two days are cropped, which only shows a repetitive tidal pattern.

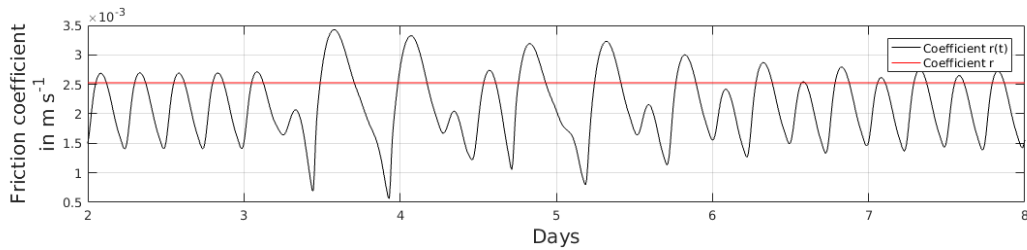


Figure 4.8: The values for the steady (red line) and time-dependent (black line) friction coefficient corresponding to surface elevations in Figure 4.7.

## 4.2 Tide-surge interaction with synthetic forcing

Figure 4.9 presents the magnitude of interaction for subcase (c) of subsection 4.1; a single channel with an open and closed boundary forced by both tide and wind. It displays the surface elevations forced simultaneously by tide and wind and elevations forced by tide and wind separately. The latter are two separate model runs where  $\zeta_{tide}$  and  $\zeta_{wind}$  are summed. By separately modelling we prevent interaction between tide and surge. The simulations forced by wind only apply a zero elevation boundary condition. The presented surface elevations are at the closed boundary. Figures 4.10 and 4.11 present the elevation difference with respectively a varying tidal phase shift and tidal duration. We apply a 90 and 180 degrees tidal phase shift. A larger tidal duration (from semi-diurnal to diurnal) means a smaller water displacement within the same time-frame. Before we point out the highlights, note that the elevations with an open boundary and wind forcing only are not plotted, but it is important to know that they reach nearly 2.5 metres.

The simulations with simultaneous forcing are at peak elevations nearly 50 centimetres lower than when separately forced. The degree of interaction increases during the ramp-up stage and decreases during the ramp-down stage of the storm surge. The varying phase differences in the tidal signal do not result in significant differences in interaction. The degree of interaction for a diurnal tide is smaller on the ramp-up side of the storm. The ramp-down side has approximate equal interaction.

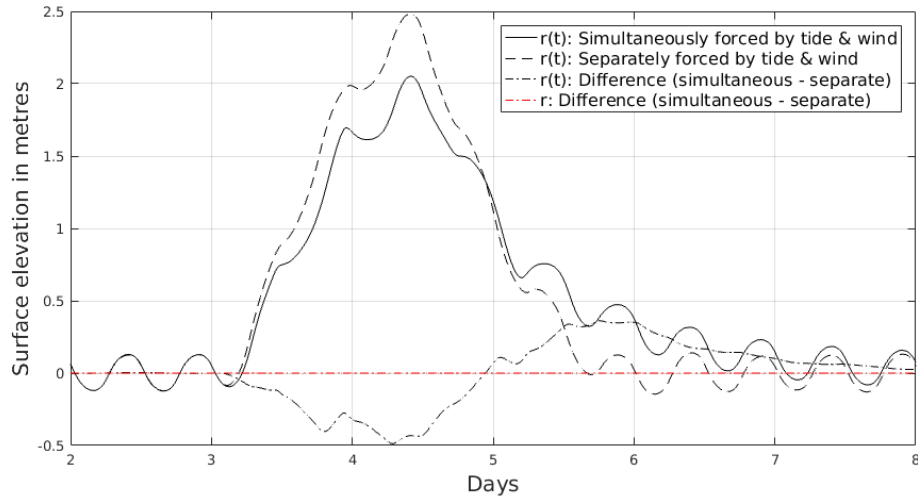


Figure 4.9: The surface elevations forced separately by tide and wind (i.e.  $\zeta_{tide} + \zeta_{wind}$ , striped black line) and the simultaneously forced (i.e.  $\zeta_{tide \text{ and } wind}$ , solid line). The difference between these two time-series is the degree of tide-surge interaction (stripe-dotted black line). The degree of tide-surge interaction with a steady friction coefficient is displayed by the red line.

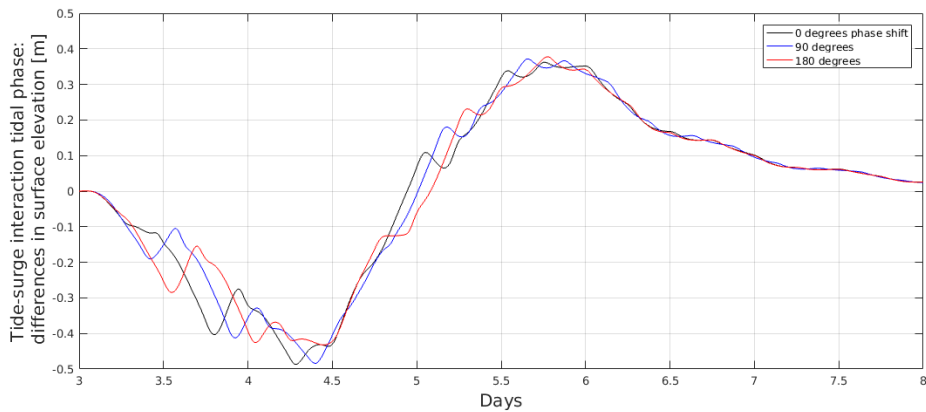


Figure 4.10: The degree of interaction for a varying tidal phase difference.

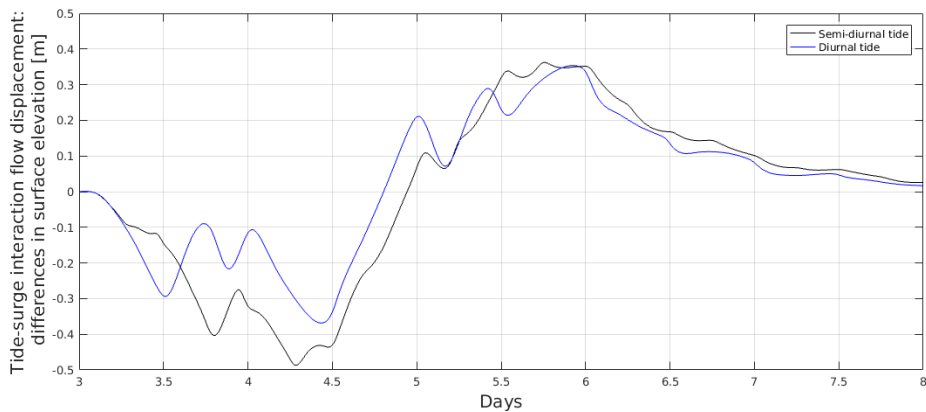


Figure 4.11: The degree of interaction for a varying tidal duration.

# Chapter 5

## Results: Wadden Sea network

### 5.1 Hindcasting Sinterklaasstorm 2013

This section presents the simulation results for the Dutch Wadden Sea network forced by the 2013 Sinterklaasstorm (both tide and wind). Subsection 5.1.1 re-simulates the model results by Reef et al. (2016) using their steady and spatially uniform coefficient  $r_j$ . Subsection 5.1.2 hindcasts the 2013 storm using the time-dependent friction coefficient  $r_j(t)$  and compares the results with observations and Reef et al.

#### 5.1.1 Re-simulating the results by Reef et al. (2016)

The model comparison between Reef et al. and this study for the same friction parametrization are shown in Figures 5.1 to 5.3. Both models apply Reef et al.'s steady and spatially uniform friction coefficient  $r_j$ , that is equation (1.1). The values of the friction coefficients are given per channel in Figure 5.4.

Both time-series show a similar elevation pattern clearly dominated by tide (semi-diurnal) and during storm also by the increased wind stress. Although one would expect nearly equal results, they are not. During high tide simulates our model generally around 10 centimetres lower and when high tide and storm coincide this can be as much as 30 centimetres. The differences at low tide are approximately the reverse of high tide. It seems that our results have a slight delay. However, this is difficult to confirm. There seems to be no delay at Harlingen, while Harlingen is the only location which differs between models. There appears to be overdamping for our model results. However, Figure 5.4 shows that our friction coefficients are not larger. The coefficients from Reef et al. are often slightly larger but approximately equal to this study, with some outliers from both models.

#### 5.1.2 Comparing $r_j(t)$ with Reef et al. (2016)

This subsection presents the performance of our time-dependent friction coefficient  $r_j(t)$  to hindcast the 2013 Sinterklaasstorm in comparison to Reef et al., who use the steady coefficient  $r_j$ . These friction coefficients are respectively given in equations 2.3 and 1.1. The simulated surface elevations for Den Oever, Kornwerderzand and Harlingen are presented in Figures 5.5 to 5.7. The values of the friction coefficients are given in Figures 5.8 and 5.9. Figures 5.10 to 5.12 zoom into the phase difference of the surface elevations. The measurements are obtained from Rijkswaterstaat (2017). Note that many remarks of subsection 5.1.1 are also applicable here.

The performance of our model to hindcast the 2013 storm is relatively good. The estimated surface elevations are close to observations. Now and then are the estimations a couple of tens of centimetres off, but they are usually within 10 centimetres. The results for Den Oever and Kornwerderzand display a lack of frictional damping. This is especially visible during high and low tide and during storm for Kornwerderzand. Peaks exceed the measurements and troughs

are estimated too low. The largest elevation differences during storm occur at Harlingen, which does not reflect a lack of frictional damping since it is underestimated. The scatter plots in Figure 5.10 to 5.12 have – besides during tidal forcing at Harlingen – an clockwise rotation as time progresses, this indicates a phase lag.

In contrast to Reef et al. are the estimated elevations not in better agreement with the observations. There is a slight improvement during storm, but the performance outside storm decreases. The phase shift is often equal or slightly less.

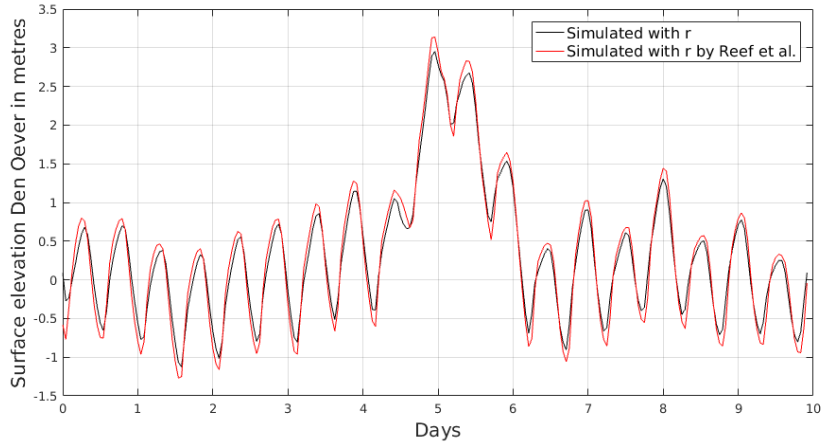


Figure 5.1: Simulated surface elevations at node D (near Den Oever) during the 2013 Sinterklaasstorm with Reef et al.'s steady friction coefficient for respectively this model (black line) and Reef et al.'s (red line). The recurrence period  $T_{recur}$  is 10 days and truncation number  $M$  is 128.

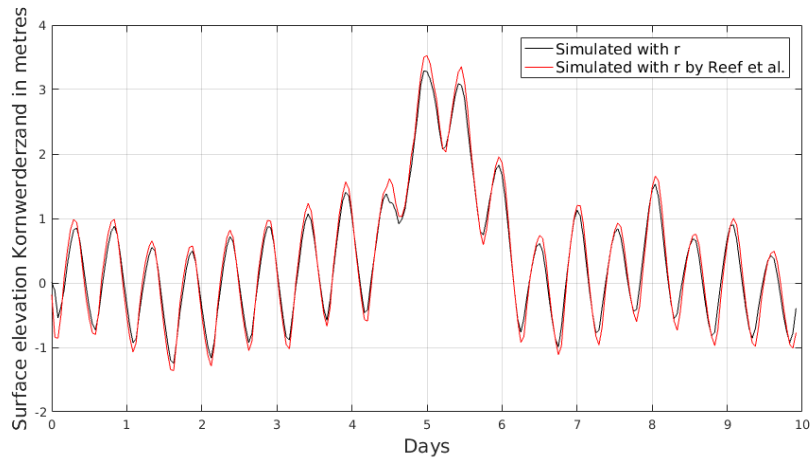


Figure 5.2: Simulated surface elevations at node E (near Kornwerderzand) during the 2013 Sinterklaasstorm with Reef et al.'s steady friction coefficient for respectively this model (black line) and Reef et al.'s (red line). The recurrence period  $T_{recur}$  is 10 days and truncation number  $M$  is 128.

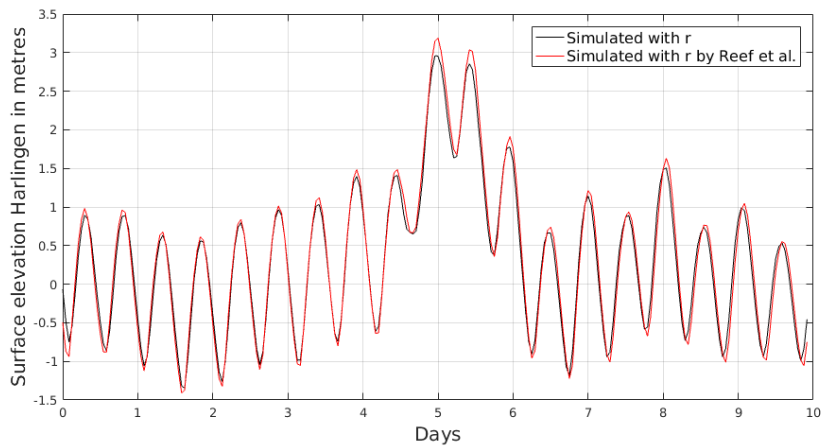


Figure 5.3: Simulated surface elevations near Harlingen during the 2013 Sinterklaasstorm with Reef et al.'s steady friction coefficient for respectively this model (black line) and Reef et al.'s (red line). The recurrence period  $T_{recur}$  is 10 days and truncation number  $M$  is 128.

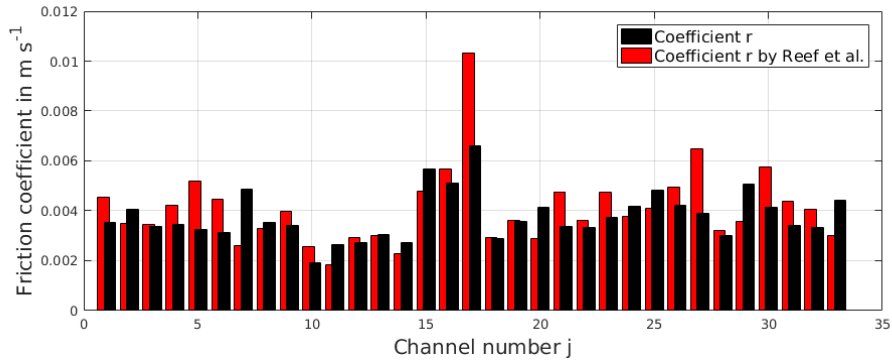


Figure 5.4: The steady friction coefficient by Reef et al. simulated with respectively this model (black bars) and Reef et al.'s (red bars) for the 2013 Sinterklaasstorm. This plot also gives an indication of  $u_{a,j}$  since the friction coefficient  $r_j$  is a product between  $gh_j^{-1/3}M_n^2$  and  $u_{a,j}$  and only the latter varies per model.

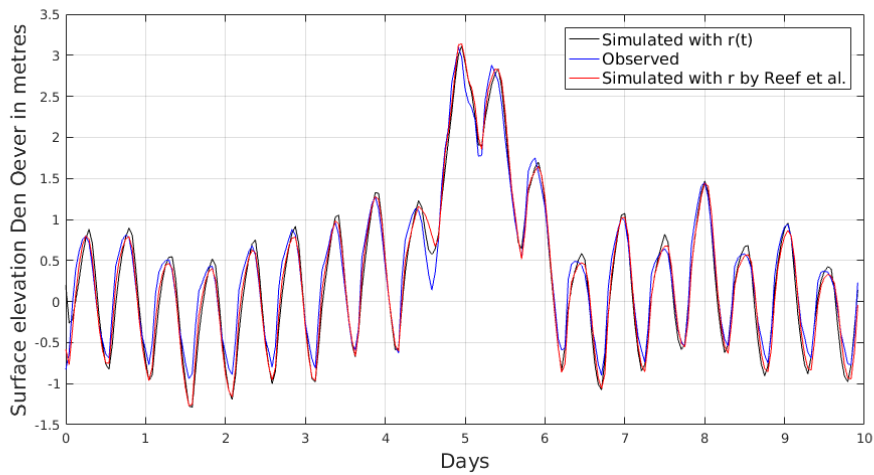


Figure 5.5: Surface elevations at node D (near Den Oever) during the 2013 Sinterklaasstorm for respectively this model with time-dependent friction coefficient  $r_j(t)$  (black line), the observed elevations (Rijkswaterstaat 2017, blue line) and Reef et al.'s (2016) model with steady coefficient  $r_j$  (red line). The recurrence period  $T_{recur}$  is 10 days and truncation number  $M$  is 128.

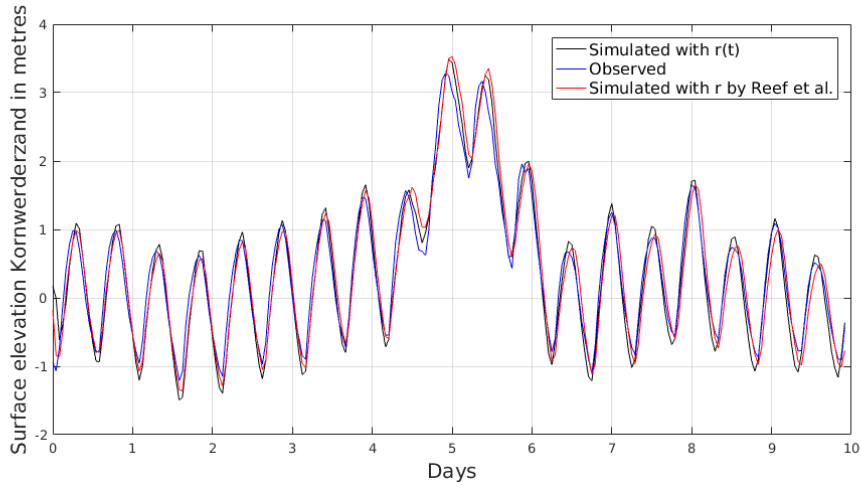


Figure 5.6: Surface elevations at node E (near Kornwerderzand) during the 2013 Sinterklaasstorm for respectively this model with time-dependent friction coefficient  $r_j(t)$  (black line), the observed elevations (Rijkswaterstaat 2017, blue line) and Reef et al.'s (2016) model with steady coefficient  $r_j$  (red line). The recurrence period  $T_{recur}$  is 10 days and truncation number  $M$  is 128.

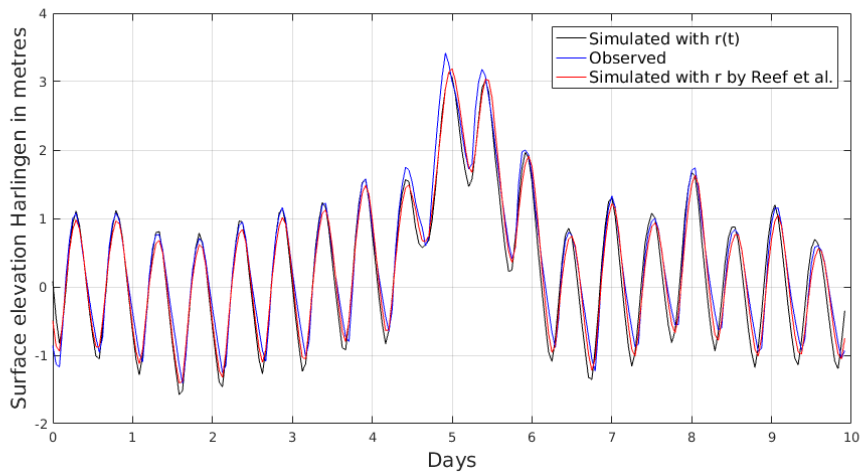


Figure 5.7: Surface elevations near Harlingen during the 2013 Sinterklaasstorm for respectively this model with time-dependent friction coefficient  $r_j(t)$  (black line), the observed elevations (Rijkswaterstaat 2017, blue line) and Reef et al.'s (2016) model with steady coefficient  $r_j$  (red line). The recurrence period  $T_{recur}$  is 10 days and truncation number  $M$  is 128.

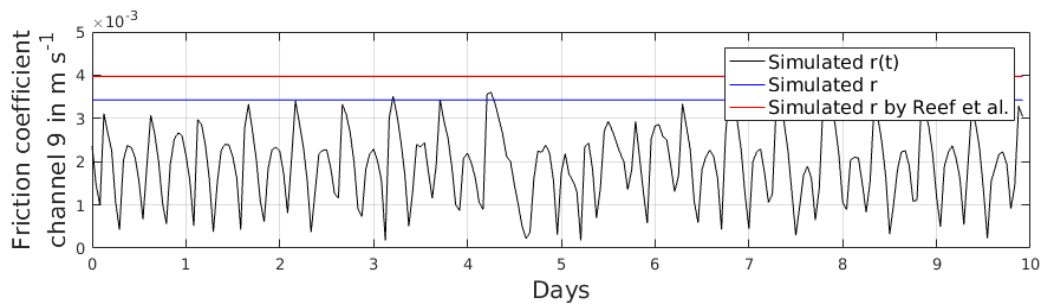


Figure 5.8: The time-series of the simulated friction coefficients for channel 9 (nodal connection DE). The black line is the friction coefficient  $r_j(t)$  and the blue line is the coefficient  $r_j$ , both result from our model. The red line is the friction coefficient  $r_j$  resulting from Reef et al. (2016). Den Oever and Kornwerderzand are respectively at the southern and norther side of this channel.

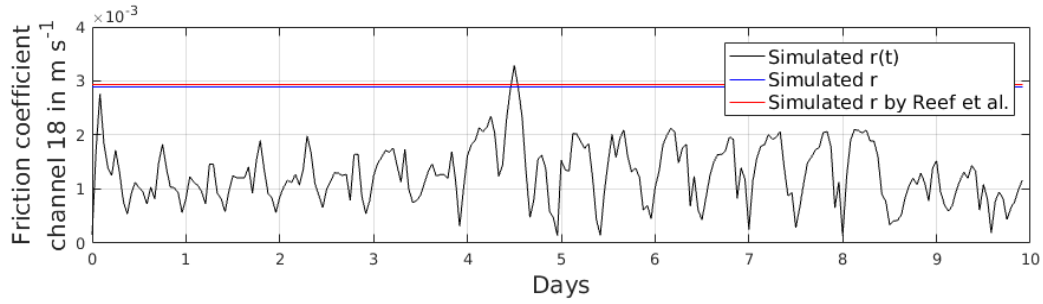
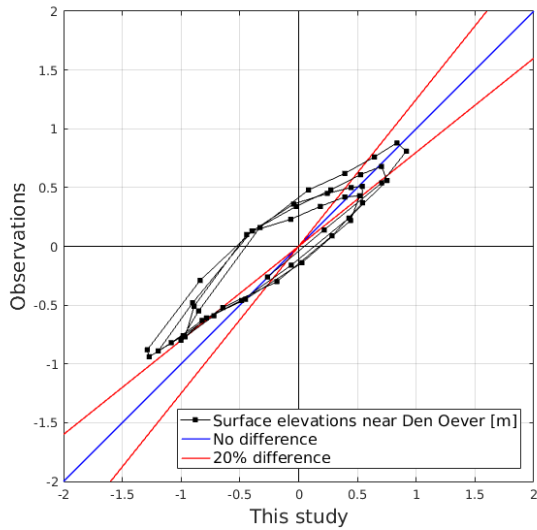
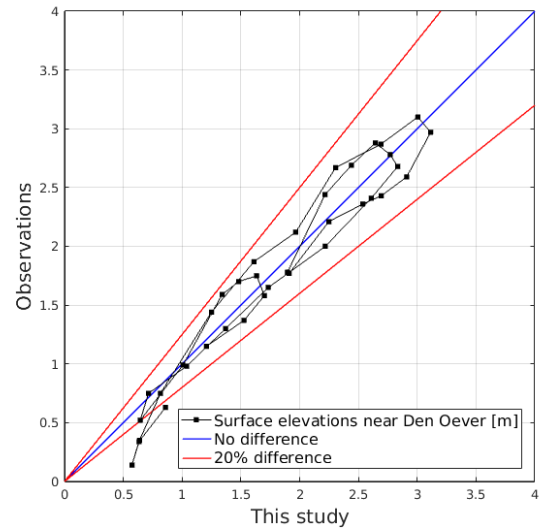


Figure 5.9: The time-series of the simulated friction coefficients for channel 18 (nodal connection FK). The black line is the friction coefficient  $r_j(t)$  and the blue line is the coefficient  $r_j$ , both result from our model. The red line is the friction coefficient  $r_j$  resulting from Reef et al. (2016). The middle point of this channel is located near measurement station Harlingen.

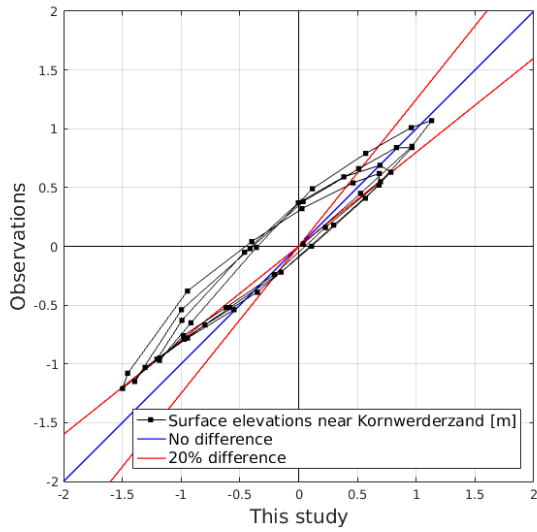


(a) Elevations Den Oever during tidal forcing

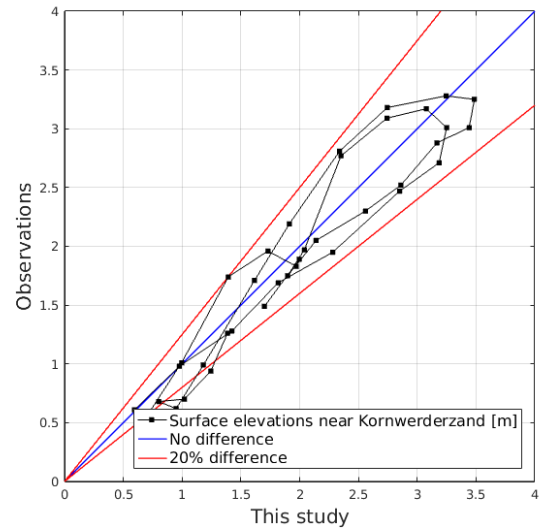


(b) Elevations Den Oever during surge

Figure 5.10: The simulated surface elevations compared to the measurements during the 2013 Sinterklaasstorm. The applied friction coefficient is the time-dependent  $r_j(t)$ . The left figure displays the elevations during two days of tide (day 1 to 3). The right figure displays the elevations during surge (day 4.5 to 6). Both elevation profiles rotate in clockwise manner as time progresses.

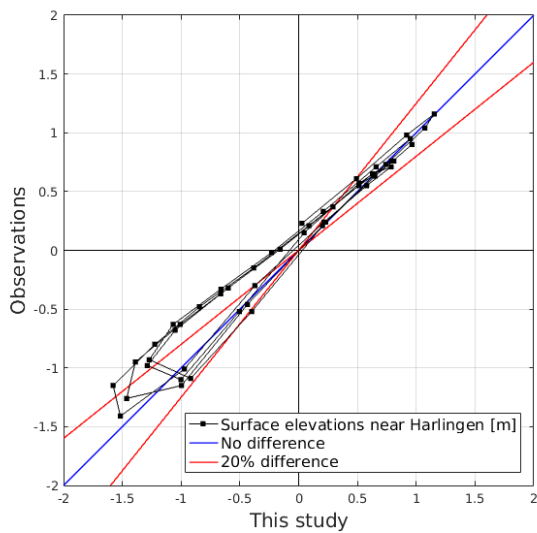


(a) Elevations Kornwerderzand during tidal forcing

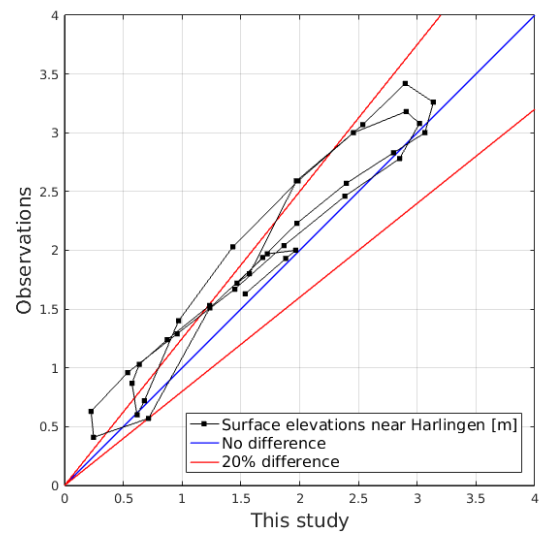


(b) Elevations Kornwerderzand during surge

Figure 5.11: The simulated surface elevations compared to the measurements during the 2013 Sinterklaasstorm. The applied friction coefficient is the time-dependent  $r_j(t)$ . The left figure displays the elevations during two days of tide (day 1 to 3). The right figure displays the elevations during surge (day 4.5 to 6). Both elevation profiles rotate in clockwise manner as time progresses. As time progresses rotates the tidal profile in a counter clockwise manner and the surge profile in a clockwise manner.



(a) Elevations Harlingen during tidal forcing



(b) Elevations Harlingen during surge

Figure 5.12: The simulated surface elevations compared to the measurements during the 2013 Sinterklaasstorm. The applied friction coefficient is the time-dependent  $r_j(t)$ . The left figure displays the elevations during two days of tide (day 1 to 3). The right figure displays the elevations during surge (day 4.5 to 6).

# Chapter 6

## Discussion

The discussion points are ordered in four sections. These are the model simplifications and assumptions in section 6.1, the solution method in section 6.2, the interpretation of the results and time-dependent friction coefficient  $r_j(t)$  in section 6.3 and the last section discusses tide-surge interaction.

### 6.1 General model simplifications and assumptions

There are several model simplifications and assumptions that are (mostly) an expected consequence of idealized modelling. Note that these simplifications and assumptions are not related to our proposed friction coefficient, but it is important to be aware of them when hindcasting real events.

First of all, we assume that the surface elevation with respect to the undisturbed water level is much smaller than the mean depth. This does not always apply and prevents the shallow water tide-surge interaction mechanism. Pugh (1987) showed that wind stress is more effective in shallow water and both Brown and Wolf (2009) and Horsburgh and Wilson (2007) showed that the residual elevation is significantly larger at low water. Alebregtse and de Swart (2016) incorporated the effect of a varying water depth by applying a perturbation expansion with a small parameter which is the ratio between the surface elevation and the depth. Alebregtse and de Swart investigated tidal propagation in combination with an imposed river discharge in an idealized model with analytical solutions. They also modelled in the frequency domain by truncating the tidal constituents. Another non-linear dynamic which was neglected is (along-channel) advection. We propose in subsection 6.2 how this can be incorporated as well.

Our model considers only one-dimensional flow. However, the surface elevation may rise above the tidal flats and with that enable cross-tidal-divide flow. This occurs especially during storm conditions. Reef et al. (2016) note that the State Committee (1926) attempted to improve this by smoothing water levels of unconnected adjacent channels. This study, and Reef et al.'s, have not attempted to do so.

The Manning roughness coefficient  $M_n$  and drag coefficient  $c_w$  are empirical. The wind stress is linearly proportional to the drag coefficient. Reef et al. note that the recommended drag value by Resio and Westerink (2008) is 25% lower than the State Committee (and this study) applied. This indicates the importance of an empirical coefficient.

Further assumptions and simplification relate to model input. For instance, the wind forcing was considered spatially uniform within the back-barrier bay, we apply a bathymetry map of the early 20th century and measurement data were only available for three out of five tidal inlets.

## 6.2 Solution method

The discussion points about the applied solution method are divided in two parts. Firstly, the points that are directly related to our proposed time-dependent friction coefficient  $r_j(t)$ . Secondly, the discussion points that would also occur without the time-dependent coefficient.

### Discussion points related to $r_j(t)$

The convolution sum couples the frequencies which cause interaction between each frequency response. This is not only interaction between tide and surge, but also interaction between tide and tide and surge and surge. This offers for instance the opportunity to investigate interaction between tidal constituents.

A simplification of the time-dependent friction coefficient is that it is spatially averaged. This would be an important simplification if there are large differences of velocity within the channel. Velocity differences increase with increasing channel length, velocity amplitude and forcing frequency. However, large frequencies tend to occur with smaller velocity amplitudes. Besides that, channel lengths of the Wadden Sea network are too small to cause significant velocity differences. Henceforth, the simplification of spatially averaging is not influential.

Where the model duration (in computational sense) was approximately proportional to the truncation number  $M$ , it is for our time-dependent friction model quadratically proportional to  $M$ . This results from the coupled frequencies in the convolution sum, which in turn couple the boundary conditions and cause quadratically larger linear algebra matrices. Depending predominantly on the required resolution and forcing length (that is  $M$ ), the model duration on a personal computer increases for the Wadden Sea network from a minute at most to approximately 10 minutes. These times are for an hourly forcing resolution. Note that an hourly resolution is essentially too coarse for tidal simulations.

### Other discussion points related to the solution method

The Fourier representation of the model output results in continuous sinusoidal signals that present the storm (or tidal) event as endlessly repeating. To prevent the repeating storm events to influence each other, we padded zeroes to the synthetic wind forcing such that the system can return to its undisturbed state before the fictitious next storm event starts. However, synthetic tidal forcing and an actual storm event – like the 2013 Sinterklaasstorm – do not (naturally) consist of padded zeroes. It is therefore important to apply a forcing time-series that is significantly larger than the storm duration, such that the period of interest is not affected.

Channel loops – like the linked nodes F, K and I in the Wadden Sea network – could result in circulating flow that is unrelated to the forcing when there is no friction. Since this is more a theoretic principle and we attempt to improve the model performance to mimic realistic cases, we did not include these type of homogeneous solutions.

We have neglected advection in the momentum equation. However, advection can be incorporated in a similar fashion to our time-dependent friction coefficient. One could replace the advection term  $\frac{\partial u}{\partial x}u$  with  $u_{ad}(t)\frac{\partial u}{\partial x}$  where  $u_{ad}(t)$  represents the advection velocity and is uniform throughout the channel. This would not complicate the convolution sum further. The coupled Helmholtz-type spatial boundary value problem changes however to a damped oscillator (a first order term appears).

## 6.3 Interpretation of results and insights from $r_j(t)$

The simulation with a single channel, closed boundaries and only wind forcing displayed underdamping when the friction coefficient approaches zero. This underdamping is a direct result of (slight) resonance in some of the higher frequencies, which is then displayed as sloshing in the elevation and velocity profile. The friction coefficient approaches zero when the surface eleva-

tion restores to its undisturbed state. It also approaches zero when the steady wind forcing and gravitational acceleration balance. This results also in underdamping. We know however that this would not occur in reality. This is a drawback of depth-averaged modelling. The surface elevation may in equilibrium, but there would occur a wind driven water circulation. This would prevent a (nearly) zero friction coefficient, and with that, prevent the underdamping. The behaviour is however in depth-averaged sense correct. Other simulations included tidal forcing and have therefore a friction coefficient that is always larger than zero. Henceforth, this resonant behaviour does not appear in the other simulations. The underdamping extends the relaxation significantly such that the fictitious next storm is still influenced by the previous.

We observe another display of time-dependent friction. The acceleration from zero flow onwards is faster than the steady friction model. This makes sense since the steady friction coefficient causes the frictional term to overestimate energy dissipation at that moment.

The simulation with a single channel, an open boundary and only tidal forcing displays excess of frictional damping for the steady friction coefficient (w.r.t. the time-dependent version). This was not directly expected since the State Committee's (1926) energy based steady friction coefficient displayed very accurate tidal estimations. We do not apply the same friction coefficient, but our steady coefficient is also energy based. Compared to the time-dependent simulations is the flow behaviour not strange though. The steady simulations accelerate more slowly and decelerate faster. This probably explains tidal phase shift and for the velocity scale the smaller maximum value and the larger range.

The time-dependent friction coefficient causes tidal asymmetry, which is especially visible in profiles of the friction coefficient and velocity scale. These profiles show respectively a steep rising side and a bump on the falling side. The steepness makes sense since a low friction allows for quick acceleration. This relation is however not visible between the velocity scale and the friction coefficient: at the start of day three we observe an increasing friction coefficient, which we would expect to correspond with an increasing velocity scale. The velocity scale decreases however. The bump in the velocity scale is also not clear. Nidzieko (2010) notes on harmonics and tidal asymmetry that this results from the non-linearities in the equations of motion, for instance advection, quadratic friction and the varying depth. The asymmetry – which results for our model from friction – is an indication of interaction between the tidal frequencies.

The simulation with a single channel, an open boundary and both tidal and wind forcing display similar phenomena as the other single channel subcases.

It would be interesting to simulate the single channel subcases with the original quadratic friction parametrization. The performance the time-dependent friction coefficient  $r_j(t)$  is for now solely based on our interpretation.

One would expect that the simulations with our Wadden Sea network model should produce equal results as Reef et al. when we apply the same steady friction coefficient. There is however a continuous excess in damping, with respect to Reef et al.'s results. It is unclear how these differences are caused. The input is equal, beside small and irrelevant differences. For example (I) the forcing time-series are one hour shorter; and (II) Reef et al. do apply the same solution method, but somewhat differently formulated. Next to that, our coupled solution method decouples correctly<sup>1</sup> and our internally determined model variables (for instance matrices  $\mathbf{B}_j$ ,  $\mathbf{P}_j$  and  $\mathbf{Q}_j$ ) possess the expected values. Reef et al.'s (Matlab) model has been searched, but not fully. When we compare our steady friction results with the time-dependent friction simulations, we observe the correct qualitative behaviour. The results from our time-dependent friction model show a good agreement with the measurements. One would therefore expect the simulations with an overestimated steady friction coefficient to be damped more.

The hindcasting results of the 2013 Sinterklaasstorm show now and then a couple of tens of centimetres difference with the measurements. The results are however usually within 10 cen-

---

<sup>1</sup> The steady friction coefficient results in a diagonal frictional matrix  $\mathbf{R}_j$ . Hence, matrix  $\mathbf{B}_j$  is also diagonal, eigen vector matrix  $\mathbf{P}_j$  is an identity matrix, eigenvalues  $\mathbf{Q}_j$  are equal to  $\mathbf{B}_j$  and thus is the system decoupled.

timetres. There is some general excess in frictional damping at Den Oever and Kornwerderzand. This is especially visible for the tidal simulations. This might indicate that the Manning roughness coefficient – which is empirical – should be somewhat larger. Reef et al. (2016) experimented with different values for the Manning coefficient. They found that a value of  $1.5M_n$  decreases the surface elevation by a couple of tens of centimetres.

The simulation results during surge are for Den Oever, Kornwerderzand and Harlingen respectively nearly perfect, overestimated and underestimated. This inconsistent behaviour possibly indicates local modulations, for instance local differences in bathymetry or wind stress. We applied the measured wind speed at the Vlieland barrier island as spatially uniform within the back-barrier bay. However, wind measurements from further inbay and inland show a decrease in wind speed, possibly explaining the overestimation at Kornwerderzand. Reef et al. (2016) appoint the overestimation at Kornwerderzand to simultaneous inflow from both adjacent network channels at Kornwerderzand. That is flow originating from the Marsdiep- and Vlie-inlet.

In contrast to Reef et al. are the estimated elevations not in better agreement with the observations. There is a slight improvement during storm, but the performance outside storm decreases. The phase shift is often equal or slightly less.

The Wadden Sea simulation does not provide additional insight in the advantages of a time-dependent friction coefficient. If the legend was not given, it would be difficult to pinpoint which time-series has a time-dependent friction coefficient and which has a steady coefficient. On the other hand, it would also be difficult to pinpoint the measurements.

The Wadden Sea simulations are performed with hourly time-series as input. This is especially for the (semi-diurnal) tide too coarse. Increasing the resolution might improve the simulation results.

## 6.4 Tide-surge interaction

We investigated the interaction between tide and surge for our single channel case, that is a channel with an open and closed boundary forced by both tide and wind. We have done this by comparing the summed elevation of two separately forced simulations with a simultaneously forced simulation.

The degree of tide-surge interaction is significant displaying a reduction of nearly 50 centimetres at peak elevations. Prandle and Wolf (1978) – who investigated interaction for the Thames estuary – mention that interaction frequently leads to a surge reduction. Although, Quinn et al. (2012) – who investigated interaction in the Solent–Southampton estuarine – note that interaction can also increase surge. Prandle and Wolf (1978) concluded that bottom friction is the dominant mechanism. We have not included other tide-surge interaction mechanisms – and thus we cannot conclude the same as Prandle and Wolf –, but tidal velocities are larger and the residual feels with that more friction. This probably explains the surge reduction.

We have performed additional simulations by varying the tidal duration and the tidal phase shift. The tidal duration was increased from a semi- to a diurnal tide. We suspected that this decreases the flow displacement within the same time frame, with that a lower tidal friction coefficient and less tide-surge interaction. We indeed observe 10 centimetres less interaction on the rising side, however, the falling side is nearly equal. The tidal phase shift did not influence the tide-surge interaction much.

# Chapter 7

## Conclusion and recommendations

### Conclusion

Concluding this study, each research question is answered below.

**1. How can we implement a time-dependent bottom friction parametrization semi-analytically without losing its linear advantages?**

The drag coefficient and absolute velocity in the quadratic friction parametrization were replaced by a linearized time-dependent friction coefficient. This friction coefficient was iteratively determined by equalling the linearized and quadratic energy dissipation. To retain the linear advantages, we transformed the friction coefficient to a Fourier series in the frequency domain. Of main interest was the resulting This resulted in product of two Fourier series; the frictional series and the output series, which in turn resulted in unequal frequencies within the momentum equation. This required us to combine the appropriate frictional and output frequencies – a convolution sum – such that each mode-dependent differential problem has an equal frequency in each term. The result is a Helmholtz-type differential problem per frequency which is coupled with all other frequencies. We addressed this by rewriting the Helmholtz-type problem in matrix notation and diagonalizing to an uncoupled Helmholtz problem using eigenvector algebra. Linear algebra subsequently allowed us to find analytical solutions per frequency, which are superposed the full solution.

**2. How do the simulation results with a time-dependent friction coefficient compare quantitatively and qualitatively with the steady coefficient for**

**a) a single channel that is synthetically forced by wind, tide and both?**

The simulations with the time-dependent friction coefficient display the qualitative behaviour corresponding to time-dependent friction. When the steady friction overestimates energy dissipation, then the time-dependent friction model displays either a faster flow acceleration or a slower deceleration. The steady friction simulations display a delay (phase shift) and overdamping compared to the time-dependent friction model. The time-dependent energy dissipation results for the tidal simulations in a clear tidal asymmetry, especially in the frictional profile. The quantitative differences resulting from simulations with both friction coefficients seem in the correct order. However, further confirmation with a fully nonlinear is preferred.

**b) Lorentz' channel network forced by the 2013 Sinterklaasstorm?**

The Wadden Sea simulation is in good agreement with measurements. The differences are often within ten centimetres. There are a couple outliers during storm of at most 30 centimetres. The results are nearly equal to the steady friction simulations by Reef et al. (2016). This is odd since the steady friction coefficient overestimates friction

significantly. The steady friction simulations by our model do show overdamping compared to the time-dependent friction simulations.

### 3. What insights do the simulation results provide for tide-surge interaction?

We have investigated tide-surge interaction for the single channel case. The simulations with simultaneous forcing result in a reduction of peak elevation compared to simulations with wind forcing only. This reduction is nearly 50 centimetres (20%). The tidal simulation consists of larger velocities and with that a larger friction coefficient, which is likely to explain the reduction. We have decreased the tidal velocities – by increasing the tidal duration – and this indeed decreases the magnitude of interaction (10 centimetres).

## Recommendations

We would like to make some recommendations for further research:

1. A fully nonlinear model can further confirm the qualitative behaviour of our solution method. The performance of the time-dependent friction coefficient  $r_j(t)$  is at this moment only based on our interpretation.
2. Our ready-to-use (Matlab) model offers the opportunity to further investigate the interaction between frequencies, for instance interaction between tidal constituents or tide and surge.

For instance, Inoue and Garrett (2007) discusses that a very weak constituent experiences 50% more friction than a strong constituent. Do we observe this in the mode-dependent (read as constituent-dependent) frictional term in equation (3.2)?

Or one could perform a harmonic analysis on the distortion of a principle constituent. Nidziko (2010) notes – while citing Friedrichs and Aubrey (1988) – on tidal distortion “*phase difference between constituents dictates the direction of asymmetry (i.e. flood or ebb dominance), while the ratio of constituent amplitudes reflects the degree of distortion*”.

3. Extending the model is our last recommendation. We have discussed the non-linear effects advection and shallow water in the discussion. Advection can be included by using the same solution method as our time-dependent friction coefficient. The perturbation expansion by Alebregtse and de Swart (2016) may incorporate shallow effects.

# Bibliography

- N.C. Alebregtse and H.E. de Swart. Effect of river discharge and geometry on tides and net water transport in an estuarine network, an idealized model applied to the Yangtze Estuary. *Continental Shelf Research*, 123:29–49, 2016. doi: 10.1016/j.csr.2016.03.028.
- W.T. Bakker and H.J. de Vriend. Resonance and morphological stability of tidal basins. *Marine Geology*, 126(1-4):5–18, 1995. doi: 10.1016/0025-3227(95)00063-5.
- M.L. Boas. *Mathematical Methods in the Physical Sciences*. 2006. ISBN 978-0-471-19826-0.
- J.M. Brown and J. Wolf. Coupled wave and surge modelling for the eastern Irish Sea and implications for model wind-stress. *Continental Shelf Research*, 29(10):1329–1342, 2009. doi: 10.1016/j.csr.2009.03.004.
- J.M. Brown, A.J. Souza, and J. Wolf. An 11-year validation of wave-surge modelling in the Irish Sea, using a nested POLCOMS WAM modelling system. *Ocean Modelling*, 33(1-2):118–128, 2010. doi: 10.1016/j.ocemod.2009.12.006.
- M.C. Buijsman and H. Ridderinkhof. Long-term ferry-ADCP observations of tidal currents in the Marsdiep inlet. *Journal of Sea Research*, 57(4):237–256, 2007. doi: 10.1016/j.seares.2006.11.004.
- W.L. Chen, P.C. Roos, H.M. Schuttelaars, and S.J.M.H. Hulscher. Resonance properties of a closed rotating rectangular basin subject to space- and time-dependent wind forcing. *Ocean Dynamics*, 65:325–339, 2015. doi: 10.1007/s10236-015-0813-2.
- W.L. Chen, P.C. Roos, H.M. Schuttelaars, M. Kumar, T.J. Zitman, and S.J.M.H. Hulscher. Response of large-scale coastal basins to wind forcing: influence of topography. *Ocean Dynamics*, 66(4):549–565, 2016. doi: 10.1007/s10236-016-0927-1.
- V.T. Chow. Open-channel hydraulics. *McGraw-Hill Book Company*, page 728, 1959. ISSN 0096-3941.
- A.T. Doodson. Report on Thames floods. *Geophysical memoirs*, 47:1–26, 1929.
- C.T. Friedrichs and D.G. Aubrey. Nonlinear tidal distortion in shallow wellmixed estuaries: A synthesis. *Estuarine Coastal Shelf Science*, 27(5):521–545, 1988.
- A.E. Hill and A.J. Souza. Tidal dynamics in channels: 2. Complex channel networks. *Journal of Geophysical Research*, 111(C11), nov 2006. doi: 10.1029/2006JC003670.
- K.J. Horsburgh and C. Wilson. Tide-surge interaction and its role in the distribution of surge residuals in the North Sea. *Journal of Geophysical Research: Oceans*, 112(C8), 2007. doi: 10.1029/2006JC004033.
- R. Inoue and C. Garrett. Fourier Representation of Quadratic Friction. *Journal of Physical Oceanography*, 37:593–610, 2007. doi: 10.1175/JPO2999.1.
- J. Klein. The North Sea storm surge atlas: Performance assessment and uncertainty analysis. Master’s thesis, University of Twente, 2015.
- KNMI. Uurgegevens van het weer in Nederland, 2017. URL <http://projects.knmi.nl/klimatologie/uurgegevens/selectie.cgi>.
- G. Lipari and G. van Vledder. Viability study of a prototype windstorm for the Wadden Sea surges. page Project A2239 by Alkyon HR&C BV for Deltares; prep, 2009.
- H.A. Lorentz. Ein Rechnungsansatz für den Widerstand bei Flüssigkeitsschwingungen. *De Ingenieur*, 37:252–254, 1922.
- N.J. Nidzieko. Tidal asymmetry in estuaries with mixed semidiurnal/diurnal tides. *Journal of Geophysical Research: Oceans*, 115(C8), 2010. doi: 10.1029/2009JC005864.
- D. Prandle and J. Wolf. The interaction of surge and tide in the North Sea and River Thames. *Geophysical Journal of the Royal Astronomical Society*, 55(1):203–216, 1978. doi: 10.1111/j.1365-246X.1978.tb04758.x.
- D.T. Pugh. Tides, surges and mean sea-level. *John Wiley & Sons*, page 472, 1987.
- N. Quinn, P.M. Atkinson, and N.C. Wells. Modelling of tide and surge elevations in the Solent and surrounding waters: The importance of tide-surge interactions. *Estuarine, Coastal and Shelf Science*, 112:162–172, sep 2012. doi: 10.1016/j.ecss.2012.07.011.
- K.R.G. Reef, P.C. Roos, G. Lipari, and S.J.M.H. Hulscher. In the footsteps of Lorentz: extending the network model of the Wadden Sea - Poster presentation. In *PECS Conference 9-14 October*, 2016.
- D. Renggli. *Seasonal predictability of wintertime wind-storm climate over the North Atlantic and Europe*. PhD thesis, Free University of Berlin, 2011.
- D.T. Resio and J.J. Westerink. Modeling the physics of storm surges. *Physics Today*, 61:33–38, sep 2008. doi: 10.1063/1.2982120.
- H. Ridderinkhof. Tidal and residual flows in the Western Dutch Wadden Sea I: Numerical model results. *Netherlands Journal of Sea Research*, 22(1):1–21, 1988a. doi: 10.1016/0077-7579(88)90049-X.
- H. Ridderinkhof. Tidal and residual flows in the western Dutch Wadden Sea II: An analytical model to study the constant flow between connected tidal basins. *Netherlands Journal of Sea Research*, 22(3):185–198, 1988b. doi: 10.1016/0077-7579(88)90022-1.
- Rijkswaterstaat. Watergegevens Rijkswaterstaat, 2017. URL <http://watergegevens.rws.nl/>.

- J.R. Rossiter. Interaction Between Tide and Surge in the Thames. *Geophysical Journal of the Royal Astronomical Society*, 6(1):29–53, dec 1961. doi: 10.1111/j.1365-246X.1961.tb02960.x.
- A.J. Souza and A.E. Hill. Tidal dynamics in channels: Single channels. *Journal of Geophysical Research*, 111(C9), sep 2006. doi: 10.1029/2006JC003469.
- State Committee. Verslag van de Staatscommissie - Gevolg van de afsluiting van de Zuiderzee. Technical Report September, 1926.
- J.Th. Thijsse. *Een halve eeuw Zuiderzeewerken 1920-1970*. 1972. ISBN 9789001860707.
- G. van Vledder and J. Adema. Hydro-dynamics in the Wadden Sea during storm conditions: Analysis of storms of 1 Nov. 2006 and 18 Jan. 2007. Technical report, Project A1848 by Alkyon HR&C BV for Deltares, prepared for Rijkswaterstaat, 2007.
- Z.B. Wang, P. Hoekstra, H. Burchard, H. Ridderinkhof, H.E. De Swart, and M.J.F. Stive. Morphodynamics of the Wadden Sea and its barrier island system. *Ocean and Coastal Management*, 68:39–57, 2012. ISSN 09645691. doi: 10.1016/j.ocecoaman.2011.12.022.

# List of symbols

- $\alpha$  Wind direction in degrees. 15, 18
- $b_j$  Channel width in  $[m]$ . 15, 18
- $\mathbf{B}_j$  The product of  $\frac{1}{gh_j} \mathbf{V}_j \mathbf{D}$  in  $[m^{-2}]$ . 26
- $\beta_j$  Channel direction in degrees. 15, 18
- $c_{d,j}$  Dimensionless drag coefficient of the quadratic friction parametrization. 20
- $c_w$  Dimensionless wind drag coefficient. 19
- $\mathbf{D}$  Time-derivative matrix in  $[rad\ s^{-1}]$ . 26
- $f_j$  Channel direction. 19
- $g$  Gravitational acceleration in  $[m\ s^{-2}]$ . 10, 18
- $H_{N,m}$  The  $m^{\text{th}}$  complex amplitude of imposed surface elevation Fourier series at node  $N$  in  $[m]$ . 23
- $h_j$  Mean water depth in  $[m]$ . 10, 15, 18
- $j$  Channel index, used as subscript for channel dependent variables. 10, 15, 18
- $J_C$  The set of adjacent channels to a node. 19
- $L_j$  Channel length in  $[m]$ . 15, 18
- $\lambda$  Eigenvalue of matrix. 26
- $M$  Truncation number, i.e. the amount of modes  $m$  (signals) in the Discrete Fourier Transformation. 23
- $m$  The mode number per signal in the Discrete Fourier Transformation. 23
- $M_n$  Manning coefficient in  $[s\ m^{-1/3}]$ . 10, 20
- $N$  Node letter. 19
- $n$  Mode  $m$ -dependent index of convolution sum.. 25
- $\omega$  The mode-dependent angular frequency of the Fourier series in  $[rad\ s^{-1}]$ . 23
- $Q_j$  Channel discharge in  $[m^3\ s^{-1}]$ . 19
- $\mathbf{Q}_j$  Diagonal eigenvalue matrix of  $\mathbf{Q}_j$ . 26
- $r_j$  Bottom friction coefficient in  $[m\ s^{-1}]$ . 10, 19
- $\mathbf{R}_j$  The frictional convolution matrix in  $[m\ s^{-1}]$ . 26
- $R_{j,m}$  The  $m^{\text{th}}$  complex amplitude of frictional Fourier series in  $[m\ s^{-1}]$ . 23
- $\rho$  Water density in  $[kg\ m^{-3}]$ . 10, 18
- $\rho_a$  Air density in  $[kg\ m^{-3}]$ . 19
- $t$  Time in  $[s]$ . 10, 18
- $\tau_{b,j}$  Bottom friction in  $[kg\ s^{-2}\ m^{-1}]$  or  $[N\ m^{-2}]$ . 18
- $\tau_w$  Spatially uniform and time-dependent wind stress in  $[kg\ s^{-2}\ m^{-1}]$  or  $[N\ m^{-2}]$ . 18
- $\mathbf{t}_j$  Vector containing the wind forcing amplitudes in  $[m^2\ s^{-2}]$ . 26
- $T_{recur}$  Storm duration, fictitious recurrence period of storm, in  $[s]$ . 21, 23
- $\mathcal{T}_{j,m}$  The  $m^{\text{th}}$  complex amplitude of wind forcing Fourier series in  $[m^2\ s^{-2}]$ . 23
- $U_{j,m}$  The  $m^{\text{th}}$  complex amplitude of velocity Fourier series in  $[m\ s^{-1}]$ . 23
- $u_{a,j}$  Velocity scale of the friction coefficient  $r_j$  by ?. Average of maximum velocity at both channel ends in  $[m\ s^{-1}]$ . 10
- $u_j$  Cross-sectionally averaged velocity in along-channel direction in  $[m\ s^{-1}]$ . 10, 18
- $u_w$  Wind speed in  $[m\ s^{-1}]$ . 18
- $\mathbf{u}_j$  Vector containing the velocity amplitudes in  $[m\ s^{-1}]$ . 26
- $\mathbf{V}_j$  The summation of  $\mathbf{D} + \frac{1}{h_j} \mathbf{R}_j$  in  $[rad\ s^{-1}]$ . 26
- $X_j$  A specific location, often channel end  $x_j = 0$  or  $x_j = L_j$ . 19
- $x_j$  Along-channel coordinate in  $[m]$ . 18
- $Z_{j,m}$  The  $m^{\text{th}}$  complex amplitude of surface elevation Fourier series in  $[m]$ . 23
- $\zeta_j$  Free surface elevation with respect to the undisturbed water level in  $[m]$ . 18

# Appendices

## Appendix A

# Example linear algebra matrices $M$ , $C$ and $A$

This appendix gives an example of the setup of the linear algebra matrices in equation (3.5) using the example network in Figure 2.1. The matrices below are respectively

- matrix  $M$  which consists of all terms dependent of the integration constants;
- vector  $C$  which consists of all integration constants;
- and vector  $A$  which consists of all terms independent of the integration constants.

